J. Fluid Mech. (1999), *vol.* 381, *pp.* 141–174. Printed in the United Kingdom

A study of the evolution and characteristics of the invariants of the velocity-gradient tensor in isotropic turbulence

By ANDREW OOI[1], JESUS MARTIN[1], JULIO SORIA[1]† AND M. S. CHONG[2]

[1]Department of Mechanical Engineering, Monash University, Melbourne, Clayton, VIC 3168, Australia
[2]Department of Mechanical and Manufacturing Engineering, University of Melbourne, Parkville, VIC 3052, Australia

(Received 7 August 1997 and in revised form 24 August 1998)

Since the availability of data from direct numerical simulation (DNS) of turbulence, researchers have utilized the joint PDFs of invariants of the velocity gradient tensor to study the geometry of small-scale motions of turbulence. However, the joint PDFs only give an instantaneous static representation of the properties of fluid particles and dynamical Lagrangian information cannot be extracted. In this paper, the Lagrangian evolution of the invariants of the velocity gradient tensor is studied using conditional mean trajectories (CMT). These CMT are derived using the concept of the conditional mean time rate of change of invariants calculated from a numerical simulation of isotropic turbulence. The study of the CMT in the invariant space (R_A, Q_A) of the velocity-gradient tensor, invariant space (R_S, Q_S) of the rate-of-strain tensor, and invariant space (R_W, Q_W) of the rate-of-rotation tensor show that the mean evolution in the (Σ, Q_W) phase plane, where Σ is the vortex stretching, is cyclic with a characteristic period similar to that found by Martin *et al.* (1998) in the cyclic mean evolution of the CMT in the (R_A, Q_A) phase plane. Conditional mean trajectories in the (Σ, Q_W) phase plane suggest that the initial reduction of Q_W in regions of high Q_W is due to viscous diffusion and that vorticity contraction only plays a secondary role subsequent to this initial decay. It is also found that in regions of the flow with small values of Q_W, the local values of Q_W do not begin to increase, even in the presence of self-stretching, until a certain self-stretching rate threshold is reached, i.e. when $\Sigma \approx 0.25 \langle Q_W \rangle^{1/2}$. This study also shows that in regions where the kinematic vorticity number (as defined by Truesdell 1954) is low, the local value of dissipation tends to increase in the mean as observed from a Lagrangian frame of reference. However, in regions where the kinematic vorticity number is high, the local value of enstrophy tends to decrease. From the CMT in the $(-Q_S, R_S)$ phase plane, it is also deduced that for large values of dissipation, there is a tendency for fluid particles to evolve towards having a positive local value of the intermediate principal rate of strain.

† Author to whom correspondence should be addressed: email julio.soria@eng.monash.edu.au.

1. Introduction

The evolution of the velocity gradient tensor (VGT) following a fluid particle is of primary importance in the understanding of the kinematics and dynamics of turbulence. Owing to its Galilean invariance property, the VGT contains significant fluid mechanics information independent of a non-accelerating observer. The dynamical behaviour of the VGT is of fundamental importance because it governs the mechanism of vortex stretching which in turn contributes to the energy cascade process in turbulent flows.

Computations of forced homogeneous isotropic turbulence can be used to study the dynamical mechanisms in the evolution of the VGT. Direct numerical simulation (DNS) of homogeneous isotropic turbulence is well established with a history of over two decades dating back to the original simulations by Orszag & Patterson (1972). Homogeneous isotropic turbulence, an idealization of general turbulent flows (including grid turbulence), assumes that all statistical properties are independent of position and all mean properties concerning a set of points are invariant under any arbitrary rotation of the set of points and the coordinate axes. Even though these are restrictive simplifying assumptions, isotropic turbulence has attracted much interest from the turbulence community because there exists sufficient work suggesting that high-Reynolds-number turbulent flows can at least be considered to be locally isotropic (see Seyed & Veeravalli 1994 and references therein). Many important features of turbulence, such as vortex stretching and viscous dissipation, are present in homogeneous isotropic turbulence and can be investigated in great detail using DNS data. These processes are representative of similar phenomena found in many common turbulent flows. An investment of effort in trying to understand the detailed properties and structure of isotropic turbulence can provide revealing insights into the physics of more realistic turbulent flows, e.g. wakes, mixing layers, jets etc.

Traditionally, analyses of DNS data have been restricted to Eulerian flow variables as it is computationally expensive to acquire Lagrangian information using DNS data. However, recent advances in supercomputer technology have allowed Yeung, Girimaji & Pope (1988), Yeung & Pope (1989), Girimaji & Pope (1990*b*) and Yeung (1994) to conduct studies related to the Lagrangian evolution of velocity gradients. As a result of these investigations, Girimaji & Pope (1990*a*), She, Jackson & Orszag (1991) and Cantwell (1992) have proposed models for the evolution of the VGT. The simplest model, known as the restricted Euler model, was first proposed in a study by Vieillefosse (1984). This model correctly reproduced some of the now well-known properties of the VGT, namely that the inclination of the intermediate rate of strain is positive (see Ashurst *et al.* 1987 and Kerr 1987), and the tendency for the vorticity vector to be parallel with the direction of the intermediate rate of strain (see Ashurst *et al.* 1987). However, Girimaji & Speziale (1995) point out that the Reynolds-averaged restricted Euler equation violates the mean momentum balance for most homogeneous turbulent flows. To overcome this problem Girimaji & Speziale (1995) proposed another model derived from the Navier–Stokes equations with a simplification similar to the restricted Euler model but imposed on the fluctuating velocity gradient field. A further shortcoming of the restricted Euler model is that its solutions become singular in finite time. In order to partially overcome this problem, Dopazo, Valiño & Martin (1993) introduced a linear model for the viscous terms in the evolution equation and showed that the resulting non-singular solutions reproduce the properties of the VGT mentioned above.

In the topological approach introduced by Chong, Perry & Cantwell (1990), the structure and evolution of the VGT, the rate-of-strain tensor and the rate-of-rotation tensor are carried out by not studying these tensors directly but by investigating their invariants. This topological methodology was first applied by Chen *et al.* (1990) to study turbulent compressible and incompressible mixing layer flows. The methodology has its roots in critical point theory (Perry & Chong 1987) and was later extended to be applicable in the interpretation of three-dimensional flows by Chong *et al.* (1990). The approach has made it possible to correlate the different invariants of the three tensors in an attempt to understand the structure of turbulent flows in a non-rotating frame of reference. Following a similar approach, the present study uses joint probability density functions (PDFs) and conditional averages to investigate the relationship between the various invariants. However, the method is extended further and an investigation of the Lagrangian dynamics of invariant quantities is conducted using the conditional mean trajectories (CMT) in invariant phase space.

This new method involves the calculation of the mean time rate of change of the invariants conditioned on the values of the invariants which gives a conditional vector field in the phase plane of an invariant pair. This conditional vector field can then be integrated to produce CMT within the phase plane of the invariant pair, allowing the mean Lagrangian dynamics of invariants of the VGT to be analysed. These trajectories are used to examine the physics of the Lagrangian evolution of the VGT.

2. Theoretical background

2.1. *Invariants of the velocity gradient tensor*

Comprehensive background material pertaining to the topological methodology can be found in Chong *et al.* (1990), Chen *et al.* (1990), Cantwell (1992), Soria *et al.* (1994), Blackburn, Mansour & Cantwell (1996) among others. Only a brief summary of the definitions and the physical meanings of the invariants will be given here.

The VGT $A_{ij} = \partial u_i/\partial x_j$ has the following characteristic equation:

$$\lambda_i^3 + P_A\lambda_i^2 + Q_A\lambda_i + R_A = 0, \tag{1}$$

where λ_i are the eigenvalues of A_{ij} and P_A, Q_A and R_A are the first, second and third tensor invariants respectively. For incompressible flows, the invariants are given by the following expressions:

$$P_A = -A_{ii} = 0, \tag{2}$$

$$Q_A = -\tfrac{1}{2}A_{ij}A_{ji}, \tag{3}$$

and

$$R_A = -\tfrac{1}{3}A_{ij}A_{jk}A_{ki}. \tag{4}$$

The local topology is only dependent on the values of Q_A and R_A. Figure 1 shows the two-dimensional (R_A, Q_A)-plane indicating the regions where the four possible non-degenerate local flow topologies (stable-focus/stretching (SF/S), unstable-focus/contracting (UF/C), stable-node/saddle/saddle (SN/S/S) and unstable-node/saddle/saddle (UN/S/S)) in incompressible flows can exist. The tent-like curve is the $D_A = 0$ line where D_A is the discriminant of A_{ij} given by

$$D_A = \tfrac{27}{4}R_A^2 + Q_A^3. \tag{5}$$

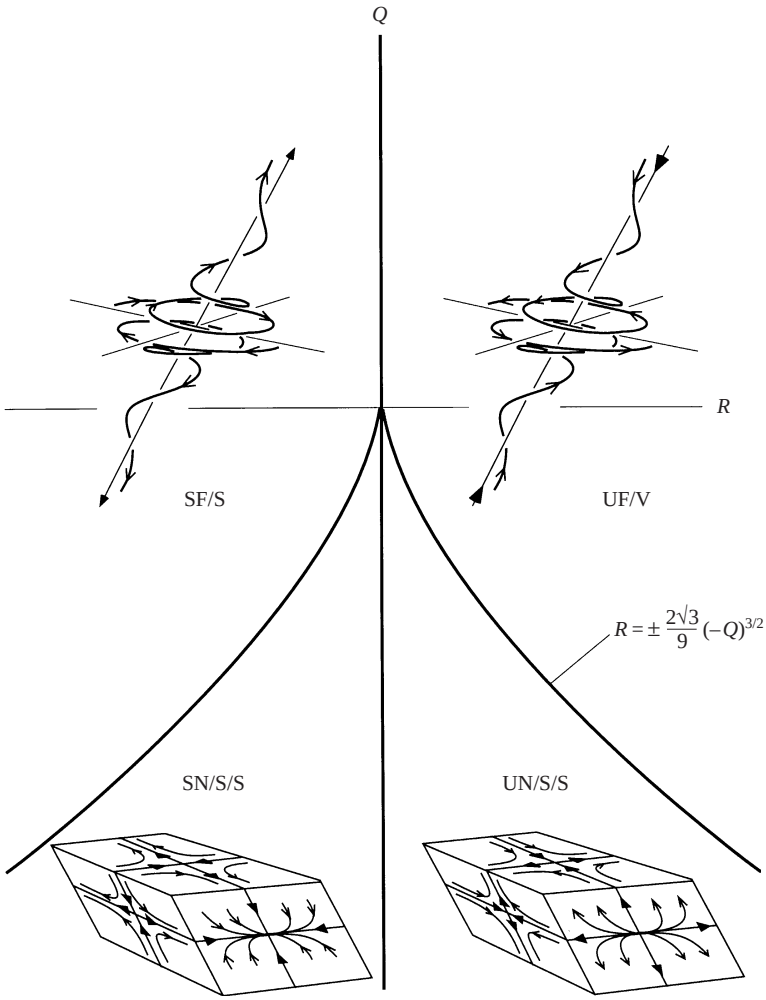

FIGURE 1. Non-degenerate local topologies for incompressible flows.

A_{ij} can be split into a symmetric and a skew-symmetric component,

$$A_{ij} = S_{ij} + W_{ij}, \tag{6}$$

where S_{ij} is the symmetric rate-of-strain tensor and W_{ij} is the skew-symmetric rate-of-rotation tensor.

In a similar fashion to the definition of the three invariants of A_{ij}, three corresponding invariants of S_{ij}, (P_S, Q_S, R_S), and the three corresponding invariants of W_{ij}, (P_W, Q_W, R_W), are defined by their respective characteristic equations. Note that $P_S = P_W = 0$ and $R_W = 0$. Q_S is negative definite while Q_W is positive definite. If α_1, α_2 and α_3 are the eigenvalues of S_{ij}, ordered such that $\alpha_1 \leqslant \alpha_2 \leqslant \alpha_3$, then

$$\mathrm{sgn}(R_S) = \mathrm{sgn}(\alpha_2), \tag{7}$$

where α_2 is the intermediate principal rate of strain.

It is sometimes convenient to describe observed phenomena in terms of the kine-

matic vorticity number introduced by Truesdell (1954) and defined as

$$\mathscr{K} = \left(\frac{Q_W}{-Q_S}\right)^{1/2}. \tag{8}$$

This quantity is a local measure of the ratio of the rotational strength to the rate of irrotational stretching of a fluid element. If $\mathscr{K} = \infty$, then the fluid particle is undergoing solid-body rotation, while fluid particles that are subjected only to irrotational stretching have a local value of $\mathscr{K} = 0$.

The stretching term in the enstrophy density transport equation is related to the third invariant of the rate-of-strain tensor and the VGT by the following equation:

$$\omega_i S_{ij} \omega_j = 4(R_S - R_A). \tag{9}$$

The rate at which the vorticity is stretched or contracted, Σ, can be expressed in terms of the invariants R_A, R_S and Q_W as

$$\Sigma = \frac{\omega_i S_{ij} \omega_j}{\omega_k \omega_k} = \frac{R_S - R_A}{Q_W}. \tag{10}$$

2.2. *Development of the evolution equations of the invariants*

In this section, evolution equations required in the computation of the CMT are developed. Following Cantwell (1992), the evolution equation for A_{ij} is easily obtained by differentiating the incompressible Navier–Stokes equations with respect to x_j, resulting in

$$\frac{\mathrm{D}A_{ij}}{\mathrm{D}t} + A_{ik}A_{kj} - (A_{km}A_{mk})\frac{\delta_{ij}}{3} = H_{ij}, \tag{11}$$

where

$$\begin{aligned} H_{ij} &= -\left(\frac{\partial^2 p}{\partial x_i \partial x_j} - \frac{\partial^2 p}{\partial x_k \partial x_k}\frac{\delta_{ij}}{3}\right) + \nu \frac{\partial^2 A_{ij}}{\partial x_k \partial x_k} \\ &= -\left(\frac{\partial^2 p}{\partial x_i \partial x_j} - \frac{2Q_A}{3}\delta_{ij}\right) + \nu \frac{\partial^2 A_{ij}}{\partial x_k \partial x_k}. \end{aligned} \tag{12}$$

H_{ij} acts like a forcing term in the evolution equation of A_{ij}.

Using the definitions of Q_A and R_A the evolution equations for Q_A and R_A are derived using (11) as

$$\frac{\mathrm{D}Q_A}{\mathrm{D}t} = -3R_A - A_{ik}H_{ki} \tag{13}$$

and

$$\frac{\mathrm{D}R_A}{\mathrm{D}t} = \tfrac{2}{3}Q_A^2 - A_{in}A_{nm}H_{mi}. \tag{14}$$

The evolution equations for Q_S and R_S are given by

$$\frac{\mathrm{D}Q_S}{\mathrm{D}t} = -3R_S + (R_S - R_A) - S_{ij}H_{ji}^S \tag{15}$$

and

$$\frac{\mathrm{D}R_S}{\mathrm{D}t} = \tfrac{2}{3}Q_S^2 + \tfrac{2}{3}Q_S(Q_A - Q_S) + \tfrac{1}{4}\mathscr{E} - S_{ij}S_{jk}H_{ki}^S, \tag{16}$$

where H_{ij}^S and H_{ij}^W are defined as the symmetric and skew-symmetric parts of H_{ij}, i.e.

$$H_{ij}^S \equiv \tfrac{1}{2}(H_{ij} + H_{ji}) = -\left(\frac{\partial^2 p}{\partial x_i \partial x_j} - \frac{2Q_A}{3}\delta_{ij}\right) + \nu \nabla^2 S_{ij} \tag{17}$$

and

$$H_{ij}^W \equiv \tfrac{1}{2}(H_{ij} - H_{ji}) = \nu\nabla^2 W_{ij}, \tag{18}$$

respectively.

$\mathscr{E}$ is the square of the vorticity stretching vector given by

$$\mathscr{E} = \left(S_{ij}\omega_j\right)\left(S_{ik}\omega_k\right). \tag{19}$$

The A_{ij} and H_{ij} terms in (13) to (16) can be calculated using data from DNS simulations and hence, $\mathrm{D}Q_A/\mathrm{D}t$, $\mathrm{D}R_A/\mathrm{D}t$, $\mathrm{D}Q_S/\mathrm{D}t$ and $\mathrm{D}R_S/\mathrm{D}t$ are known on every point in the computational grid. The evolution equation for $\mathrm{D}Q_W/\mathrm{D}t$ can be deduced using the kinematic relationship

$$Q_W = Q_A - Q_S, \tag{20}$$

which gives

$$\frac{\mathrm{D}Q_W}{\mathrm{D}t} = 2(R_S - R_A) + W_{ij}H_{ji}^W. \tag{21}$$

The evolution equation for $\mathscr{E}$ follows from its definition, i.e.

$$\frac{\mathrm{D}\mathscr{E}}{\mathrm{D}t} = -\tfrac{16}{3}\left(R_S - R_A\right)Q_A + 2S_{ij}\omega_j\left(H_{il}^S\omega_l + S_{ik}\omega_k^H\right), \tag{22}$$

where ω_k^H refers to the vector derivable from the skew-symmetric part of H_{il}, i.e.

$$\omega_i^H \equiv \epsilon_{ijk}H_{kj}^W = \nu\nabla^2\omega_i. \tag{23}$$

The quotient rule is used to develop the evolution equation for Σ which is given as

$$\begin{aligned}\frac{\mathrm{D}\Sigma}{\mathrm{D}t} = \frac{1}{Q_W^2}(&2Q_WQ_S^2 + \tfrac{2}{3}Q_SQ_W^2 - \tfrac{2}{3}Q_A^2Q_W - 2(R_S - R_A)^2 + \tfrac{1}{4}\mathscr{E}Q_W \\ &-H_{ij}^SS_{jl}S_{li}Q_W + A_{in}H_{nm}H_{mi}Q_W - H_{ij}W_{ij}(R_S - R_A)).\end{aligned} \tag{24}$$

Although $\mathscr{E}$ is not an invariant of a tensor, it is a Galilean invariant quantity like the tensor invariants – thus, for brevity all variables which are Galilean invariant will also be referred to simply as invariant quantities.

2.2.1. *The effect of H_{ij} on the evolution of invariant quantities*

The properties of H_{ij} need to be understood in order to develop a mathematical model for the evolution of invariant quantities described in the previous section. An initial attempt to study the properties of H_{ij} via its invariants for the case of decaying isotropic turbulence and a temporally evolving plane wake has been undertaken by Cheng (1996). However, only joint PDFs were computed in this study and hence only the kinematic effect of H_{ij} was studied.

In order to develop a full dynamical model for H_{ij}, there is a need to study and understand the full effect of the H_{ij} tensor on the Lagrangian dynamics of the invariants. This type of study requires well-resolved data to evaluate all the right-hand-side terms in the evolution equations. Accurate spatial derivatives of the velocity and pressure field are needed. For this reason, spectral simulation of homogeneous isotropic turbulence seems the most appropriate flow to provide the data. The data for both decaying and forced homogeneous turbulence were computed using the spectral code described in the next section.

3. Details of the direct numerical simulation

The data for this investigation were obtained from simulations of forced isotropic turbulence. The forcing was achieved by adding energy into the lower-wavenumber components to ensure that the volume-averaged kinetic energy does not decay. A variety of methods (forcing schemes) have been put forward by Siggia & Patterson (1978), Eswaran & Pope (1988), Vincent & Meneguzzi (1991), Jiménez *et al.* (1993) and Sullivan, Mahalingam & Kerr (1994) to inject energy into the lower-wavenumber components. The forcing scheme used in this work is similar to that introduced by Eswaran & Pope (1988) where energy is injected into the lower-wavenumber Fourier modes of the Navier–Stokes equations using the Uhlenbeck–Ornstein statistical process.

The Navier–Stokes equations in Fourier space are given as

$$\frac{\mathrm{d}}{\mathrm{d}t}\hat{\boldsymbol{u}}(\boldsymbol{k}) = \hat{\boldsymbol{a}}(\boldsymbol{k}), \tag{25}$$

where $\hat{\boldsymbol{a}}(\boldsymbol{k})$ is the Fourier transform of the sum of the convection, viscous and pressure gradient terms in the Navier–Stokes equations. To ensure that the volume-averaged kinetic energy does not decay with time, a forcing acceleration term is added to the lower wavenumber components of (25), hence

$$\frac{\mathrm{d}}{\mathrm{d}t}\hat{\boldsymbol{u}}(\boldsymbol{k}) = \hat{\boldsymbol{a}}(\boldsymbol{k}) + \hat{\boldsymbol{a}}^F(\boldsymbol{k}). \tag{26}$$

Here $\hat{\boldsymbol{a}}^F(\boldsymbol{k})$ is the forcing term which is non-zero only for wavenumbers $\boldsymbol{k}$ within the band $0 < k \leqslant K_F$ where $k = |\boldsymbol{k}|$ and K_F is the cut-off wavenumber. The forcing acceleration $\hat{\boldsymbol{a}}^F(\boldsymbol{k})$ is based on the Uhlenbeck–Ornstein statistical process with the real and imaginary parts of each component of $\hat{\boldsymbol{a}}^F(\boldsymbol{k})$ generated independently. Thus, at each wavenumber there are six independent Uhlenbeck–Ornstein processes. Each of these has a variance of σ^2 and a time scale T_L. These six processes are combined to form the complex forcing vector $\hat{\boldsymbol{b}}(\boldsymbol{k})$ (see Yeung *et al.* 1988). In general $\hat{\boldsymbol{b}}(\boldsymbol{k})$ does not satisfy continuity, thus continuity must be imposed by projecting $\hat{\boldsymbol{b}}(\boldsymbol{k})$ onto a plane that is normal to the wavevector $\boldsymbol{k}$, i.e.

$$\hat{\boldsymbol{a}}^F(\boldsymbol{k}) = \hat{\boldsymbol{b}}(\boldsymbol{k}) - \boldsymbol{k}\frac{\boldsymbol{k}\cdot\hat{\boldsymbol{b}}(\boldsymbol{k})}{\boldsymbol{k}\cdot\boldsymbol{k}}, \tag{27}$$

This provides the required forcing acceleration $\hat{\boldsymbol{a}}^F(\boldsymbol{k})$ which also satisfies the continuity constraint, i.e. $\boldsymbol{k}\cdot\hat{\boldsymbol{a}}^F(\boldsymbol{k}) = 0$.

The following statistical quantities were calculated and stored at every time step during the simulation:

$l = \dfrac{\pi}{2u_{rms}^2}\displaystyle\int_0^{k_{max}} \frac{E(k)}{k}\mathrm{d}k$, the integral length scale where u_{rms} is the rms velocity;

$\lambda = \left(\dfrac{\langle u_\alpha^2\rangle}{\left\langle \left(\partial u_\alpha/\partial x_\alpha\right)^2\right\rangle}\right)^{1/2} = \left(\dfrac{5\langle u_i u_i\rangle}{\langle \omega_i\omega_i\rangle}\right)^{1/2}$, the Taylor microscale;

$\eta = \left(\nu^3/\epsilon\right)^{1/4}$, the Kolmogorov microscale;

the volume − averaged kinetic energy of the flow;

the volume − averaged dissipation of the flow;

$F_3(u_\alpha)$, the skewness of any one velocity component;

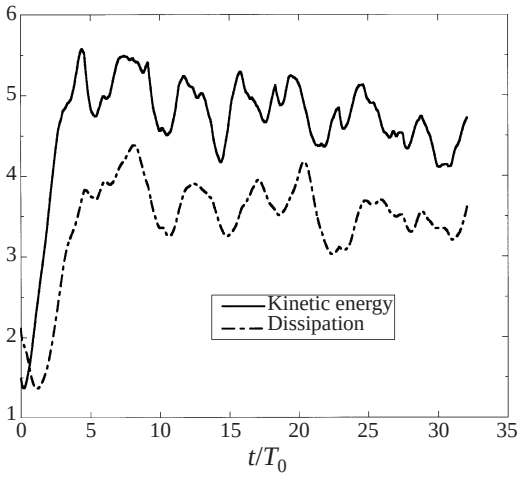

FIGURE 2. Time evolution of mean kinetic energy and ϵ in the simulation of forced isotropic turbulence at $Re_\lambda = 41.5$.

$F_4(u_\alpha)$, the kurtosis of any one velocity component;
$F_3(\omega_\alpha)$, the skewness of any one component of vorticity;
$F_4(\omega_\alpha)$, the kurtosis of any one component of vorticity.

The operator F_n is defined as

$$F_n(T) = (-1)^n \frac{\langle T^n \rangle}{\langle T^2 \rangle^{n/2}}. \tag{28}$$

The temporal evolution of some of these quantities for the case at $Re_\lambda = 41.5$ is shown in figures 2 and 3. Figure 2 shows the evolution of the volume-averaged kinetic energy and dissipation with time non-dimensionalized by the eddy-turnover time,

$$\tau_{eddy} = l/u_{rms}. \tag{29}$$

The volume-averaged kinetic energy and dissipation pass through an initial transient state but eventually reach a steady state where they oscillate about some mean value. The time evolution of the skewness and kurtosis of u_α and ω_α are shown in figure 3. The kurtosis of u_α remains approximately constant at 2.8 while the kurtosis of ω_α increases and subsequently oscillates about a mean value. This result agrees well with the kurtosis value of between 2.9 and 3.0 reported by Batchelor (1960) for experimental data of grid turbulence. The skewness for both u_α and ω_α remain approximately zero throughout the simulation, which also agrees with the reported value of zero by Batchelor (1960) for experimental grid turbulence data.

Further pertinent parameters of the three simulations which are used to provide the data for this investigation are tabulated in table 1. All simulations were continued for a sufficiently long time for the instantaneous integral characteristics to become statistically steady, which typically took several large-eddy turnover times. The data shown in table 1 are ensemble averages, i.e. space- and time-averaged quantities. The calculation of time averages of the data was only undertaken after the simulations had reached a statistically steady state. Table 1 shows that u_α has a skewness value of approximately zero and a flatness value of approximately 2.8 for all three simulations and is in good agreement with experimental data (Batchelor 1960).

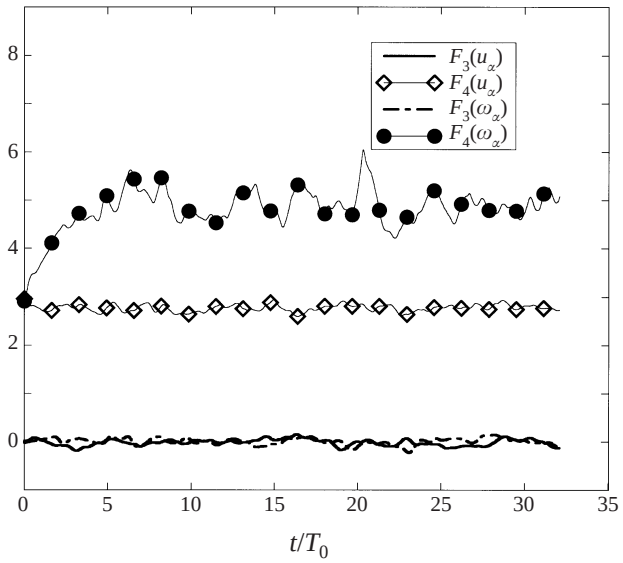

FIGURE 3. Time evolution of skewness and kurtosis of u_α and ω_α for the simulation of forced isotropic turbulence at $Re_\lambda = 41.5$.

Re_λ	41.5	48.2	70.9
L	2π	2π	2π
ν	0.025	0.025	0.025
k_0	1	1	1
N	64	96	128
K_F	$2\sqrt{2}$	$2\sqrt{2}$	$2\sqrt{2}$
ϵ	3.6	8.33	57.5
u_{rms}	1.8	2.4	4.7
l	1.1	1.0	1.0
λ	0.58	0.51	0.38
η	0.046	0.037	0.023
t_η	0.083	0.055	0.021
$\Delta t/t_\eta$	0.012	0.009	0.024
$k_{max}\eta$	1.7	2.0	1.7
l/L	0.18	0.17	0.17
$F_3(u_\alpha)$	0.0	0.0	0.0
$F_4(u_\alpha)$	2.8	2.9	2.8
$F_3(\omega_\alpha)$	0.0	0.0	0.0
$F_4(\omega_\alpha)$	4.9	5.3	6.2
S_ϵ	0.521	0.523	0.505
$\epsilon l/u_{rms}^3$	0.65	0.61	0.53

TABLE 1. Parameters of simulations and calculated Eulerian flow variables.

To ensure good spatial resolution $k_{max}\eta$ must be greater than 1, where η is the Kolmogorov microscale representing the dissipation scale and hence the smallest significant turbulence scale, while k_{max} is the maximum wavenumber in the simulation, which indicates the smallest scale that can be resolved in the simulation, which is of the order $1/k_{max}$. Table 1 indicates the respective values for $(k_{max}\eta)$ for all simulation cases presented here. The computational domain of the simulation is periodic, hence

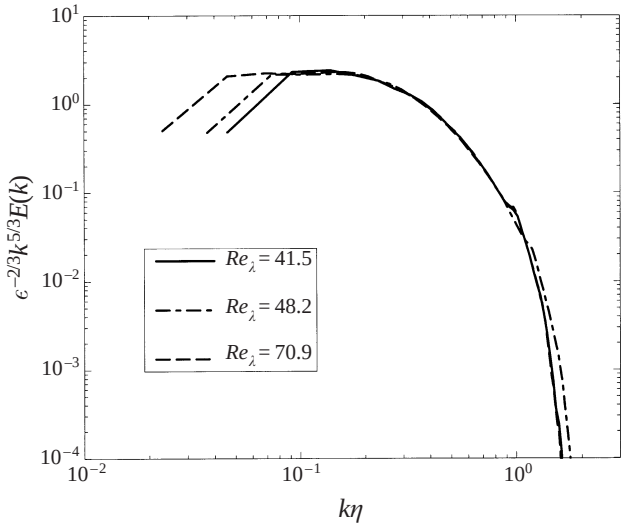

FIGURE 4. Three-dimensional energy spectra for the three different Re_λ cases used in this paper. The horizontal region displays the inertial range in each case.

to ensure that all significant length scales in the flow are not contaminated by the periodicity of the computational domain the ratio l/L should be as small as possible. For the simulations reported here, $l/L < 0.18$. The Kolmogorov time scale defined by

$$t_\eta = (\nu/\epsilon)^{1/2}, \tag{30}$$

is representative of the smallest time scale in turbulent flows. Hence to ensure that t_η is well resolved, the ratio $\Delta t/t_\eta$ must be small. Table 1 shows that for all simulations $\Delta t/t_\eta < 0.025$.

Three-dimensional shell-averaged energy spectra for the three cases providing the data base for this study are presented in figure 4. All cases show a short inertial range with a power decay of approximately $k^{-5/3}$. It is clearest in the highest Re_λ case used for this investigation. There is a satisfactory collapse of the spectra in the dissipation range, although, as observed by other investigators (see Jiménez *et al.* 1993) the dissipation spectra at the higher Re_λ appear fuller. The Kolmogorov constant in the inertial range is found to be approximately equal to 2.0 and is in good agreement with the value found by others (see Jiménez *et al.* 1993).

4. Conditional mean rate of change of invariants.

In order to study the mean temporal evolution of the invariants it is necessary to consider the temporal evolution for different ensembles of fluid particles with a given set of specified initial conditions. This process requires accurate simultaneous particle tracking of a large number of particles during the turbulence simulation to acquire sufficient statistical data. This type of computation requires a large amount of CPU time which was not available to the authors. An alternative approach is to consider the mean temporal rate of change of the velocity gradient invariants which can be determined using a conditional average technique.

The conditional mean rate of change of an invariant pair (X, Y) is numerically computed using the following discrete formulae:

$$\dot{X}(X,Y) \equiv \left\langle \frac{\mathrm{D}X}{\mathrm{D}t} \middle| (X = X_0, Y = Y_0) \right\rangle = \frac{1}{N_{XY}} \sum_{X_0-\Delta_X/2}^{X_0+\Delta_X/2} \sum_{Y_0-\Delta_Y/2}^{Y_0+\Delta_Y/2} \frac{\mathrm{D}X}{\mathrm{D}t}(X,Y), \quad (31)$$

$$\dot{Y}(X,Y) \equiv \left\langle \frac{\mathrm{D}Y}{\mathrm{D}t} \middle| (X = X_0, Y = Y_0) \right\rangle = \frac{1}{N_{XY}} \sum_{X_0-\Delta_X/2}^{X_0+\Delta_X/2} \sum_{Y_0-\Delta_Y/2}^{Y_0+\Delta_Y/2} \frac{\mathrm{D}Y}{\mathrm{D}t}(X,Y), \quad (32)$$

where Δ_X is the bin width in the X variable, Δ_Y is the bin width in the Y variable, and N_{XY} is number of samples in the domain of $X_0 - \Delta_X/2 < X < X_0 + \Delta_X/2$ and $Y_0 - \Delta_Y/2 < Y < Y_0 + \Delta_Y/2$. The $\langle\ \rangle$ brackets represent the ensemble mean of $\mathrm{D}X/\mathrm{D}t$ or $\mathrm{D}Y/\mathrm{D}t$ at $(X = X_0,\ Y = Y_0)$.

An illustration of the computational technique and issues relating to statistical convergence are presented for R_A and Q_A. Corresponding computations and the discussion of convergence issues for all other invariant pairs are similar. Since all terms on the right hand-sides of (13) and (14) can be calculated at every point in the flow field, both $\mathrm{D}Q_A/\mathrm{D}t$ and $\mathrm{D}R_A/\mathrm{D}t$ are calculable at every point in the flow field. In order to calculate the average values of $\mathrm{D}Q_A/\mathrm{D}t$ and $\mathrm{D}R_A/\mathrm{D}t$ conditioned upon R_A and Q_A, the (R_A, Q_A) phase plane is firstly divided into $N_R \times N_Q$ equally sized bins, where N_R is the number of bins in the R_A coordinate and N_Q is the number of bins in the Q_A coordinate. The average values of $\mathrm{D}Q_A/\mathrm{D}t$ and $\mathrm{D}R_A/\mathrm{D}t$ are then computed at every bin in the (R_A, Q_A) phase plane using (31) and (32) with R_A replacing X and Q_A replacing Y. The conditional mean values of $\mathrm{D}R_A/\mathrm{D}t$ and $\mathrm{D}Q_A/\mathrm{D}t$ are therefore known for every bin in the (R_A, Q_A) phase plane and represent a conditional mean vector field $(\dot{R}_A(R_A, Q_A), \dot{Q}_A(R_A, Q_A))$ in the (R_A, Q_A) phase plane.

The conditional mean trajectories (CMT) in the (R_A, Q_A) phase plane are computed using the conditional mean vector field. The same procedure is applied to calculate the conditional vector field and corresponding CMT for the $(Q_W, -Q_S)$, (R_S, Q_S), (Σ, Q_W) and $(\Sigma, -Q_S)$ phase planes. The convergence of the conditional mean vector fields of the (R_A, Q_A) invariants was investigated to ensure their statistical convergence. Figures 5(*a*) and 5(*b*) show $\dot{Q}_A(R_A, Q_A)$ and $\dot{R}(R_A, Q_A)$ evaluated at point P (shown in figure 6) as a function of the number of samples. These two figures show that convergence of the conditional means is achieved if more than 300 samples per bin are used.

The resolution of the CMT is dependent on the bin size. As expected, there is an improvement in the resolution of the computed CMT for smaller bin size. However, if the bin size is too small there is insufficient sample data available in a given bin for the statistics to converge. This problem is illustrated in figure 7(*a*) which shows the function $\dot{Q}_A(Q_A = 0, R_A)$ computed using different bin sizes. For large bin sizes, the function $\dot{Q}_A(Q_A = 0, R_A)$ is poorly approximated. As the bin size is decreased, the function $\dot{Q}_A(Q_A = 0, R_A)$ is better approximated as demonstrated by the collapse of the data in the range $-2 < R_A < 2$ for bin sizes 0.8×0.8, 0.4×0.4 and 0.2×0.2. Smaller bin sizes result in wild oscillations in $\dot{Q}_A(Q_A = 0, R_A)$ for large values of $R_A/\langle Q_W \rangle^{3/2}$. This is a direct result of a lack of samples in the bins. A similar behaviour is found for $\dot{Q}_A(Q_A, R_A = 0)$ as shown in figure 7(*b*). This plot shows convergence for bin sizes 0.8×0.8, 0.4×0.4 and 0.2×0.2 as indicated by the collapse of the $\dot{Q}_A(Q_A, R_A = 0)$ data in the range $-2 < (Q_A/\langle Q_W \rangle) < 6$.

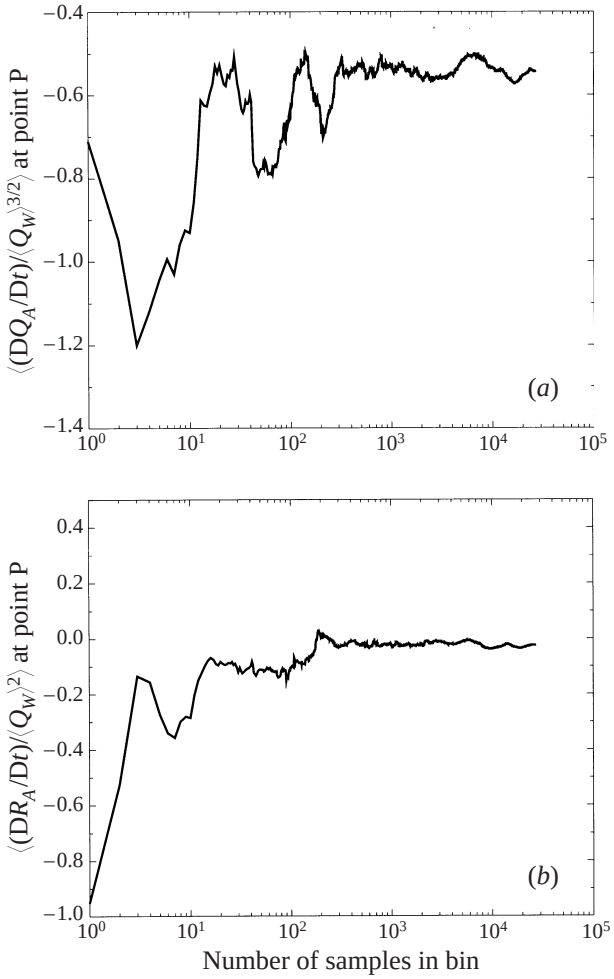

FIGURE 5. The convergence of the statistics of the conditional means (*a*) $\langle DQ_A/Dt|R_A, Q_A\rangle$, and (*b*) $\langle DR_A/Dt|R_A, Q_A\rangle$, at point P shown in figure 6.

5. Results and discussion

5.1. *Joint PDFs of invariants and related data*

In this section, joint PDFs are utilized to investigate the structure of the invariants and the geometry of turbulent motions in isotropic turbulence. Unless otherwise stated, all results presented in this paper correspond to DNS data of forced isotropic turbulence at $Re_\lambda = 70.9$. The joint PDF of R_A vs. Q_A shown in figure 8(*a*) indicates that most of the flow domain has small gradients, confirmed by the maximum of the joint PDF lying around the origin. The different contour levels have a self-similar 'pear' shape, indicating that most data points in the flow have a local topology which is either SF/S or UN/S/S. There is a tendency for the data to 'hug' the $D_A = 0$ line when the local topology of the flow is UN/S/S. Similar results were found in the study of the plane mixing layer by Soria *et al.* (1994), the channel flow by Blackburn *et al.* (1996) and the turbulent boundary layer by Chong *et al.* (1998). One of the most interesting features to be noted is that although the large-scale motions of these simulations are different due to the different global flow geometries, the joint PDFs

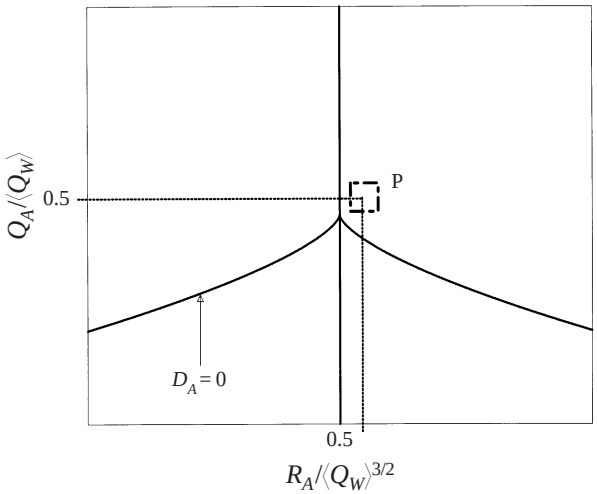

FIGURE 6. The point P where the statistical convergence of $\langle \mathrm{D}Q_A/\mathrm{D}t|R_A, Q_A\rangle$ and $\langle \mathrm{D}R_A/\mathrm{D}t|Q_A, R_A\rangle$ were checked in figure 5.

of R_A vs. Q_A are similar for all these flows. This suggests a kind of universality in the (R_A, Q_A) invariant space for all motions of turbulence.

Figure 8(*b*) shows the joint PDF of Q_W vs. $-Q_S$. The physical meaning of different regions in the joint PDF of Q_W vs. $-Q_S$ can be found in Perry & Chong (1994). A self-similar shape of the contour levels is also observed here. The joint PDF is slightly skewed towards the axis, with high Q_W indicating that the highest local value of $-Q_S$ is smaller than the highest local value of Q_W in the flow field. This suggests that flow regions with high Q_W resemble solid-body rotation with little energy dissipation and hence should be relatively long lived. In fact, for all times in the simulations, it was observed that the maximum value of Q_W is about at least a factor of 2 to 3 higher than the maximum value of $-Q_S$. This result is in agreement with that found by Yeung & Pope (1989) in their isotropic turbulence data.

Figure 8(*c*) shows the joint PDF of R_S vs. Q_S. Since S_{ij} is a symmetric tensor, the joint PDF for the invariants R_S vs. Q_S can only lie below the null discriminant curve, i.e.

$$D_S = (27/4)R_S^2 + Q_S^3 = 0. \tag{33}$$

The contour lines of this joint PDF also have a self-similar shape with a strong preference for $R_S > 0$, indicating that most data points in the flow have $\alpha_2 > 0$. A more detailed analysis of all three data bases of isotropic turbulence reveals that approximately 80% of all points in the flow have $\alpha_2 > 0$. Physically, this means that most flow regions are stretched in two orthogonal directions and contracted in the third. Figure 8(*c*) also shows that data points in the flow which have high values of $-Q_S$ also have positive α_2.

The joint PDFs for Σ vs. $-Q_S$ and Σ vs. Q_W are shown in figures 8(*d*) and 8(*e*) respectively. It is evident from these two figures that most points in the flow have positive values of Σ, i.e. the vorticity vectors are being stretched. The highest values of $-Q_S$ and Q_W can be seen to be associated with positive values of Σ. In figure 8(*e*), high stretching rates, Σ, are associated with regions where Q_W is small and *not* with regions of high Q_W. This was interpreted by Jiménez *et al.* (1993) to imply that there is little evidence of self-stretching by structures in the flow field which have large

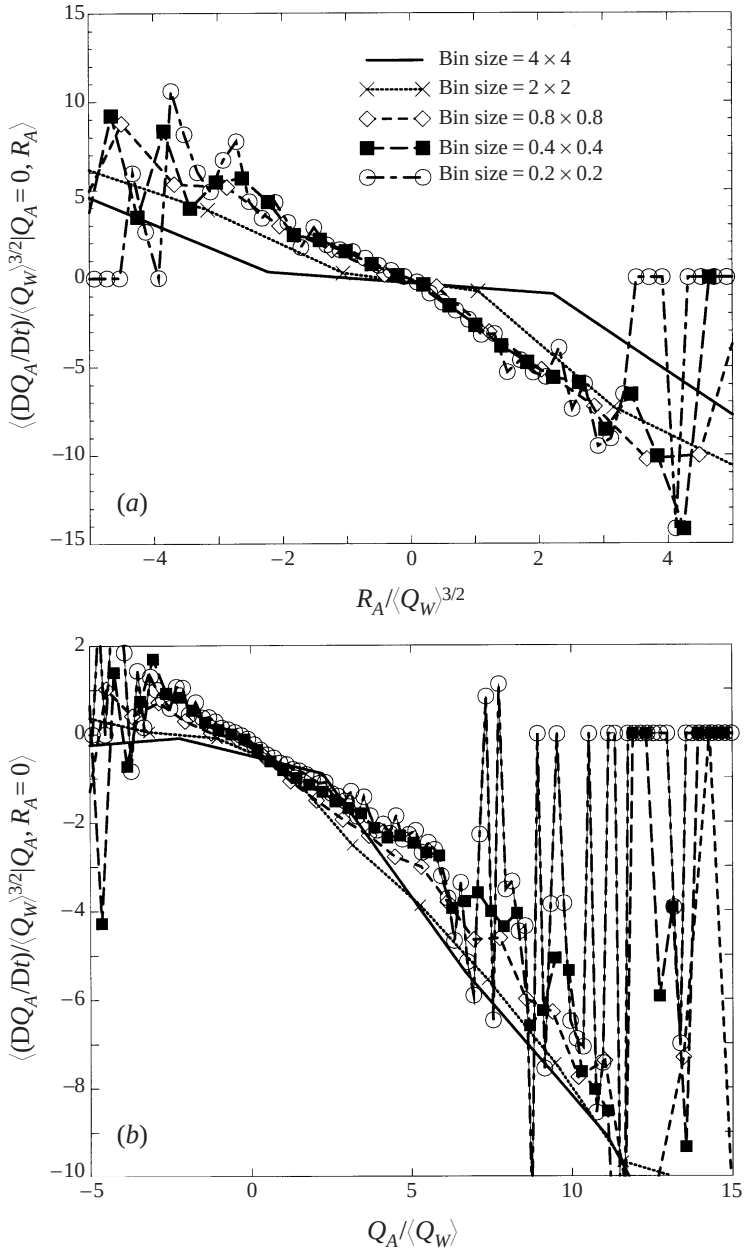

FIGURE 7. The dependence of (*a*) $\langle DQ_A/Dt|Q_A = 0, R_A\rangle$ (using data from forced isotropic turbulence), and (*b*) $\langle DQ_A/Dt|R_A, Q_A = 0\rangle$ (using data from forced homogeneous isotropic turbulence), at $Re_\lambda = 48.2$, on the bin size.

values of Q_W (the dynamics will be discussed in §5.2). The joint PDF of Σ vs. $-Q_S$ shown in figure 8(*d*) has a small base growing wider for larger values of $-Q_S$. This indicates that the largest $|\Sigma|$ in the flow is associated with regions of moderate to high $-Q_S$.

Figure 9 shows the significance of regions with positive D_A. Three curves are plotted on this graph showing: (i) the amount of the flow volume with $D_A > D_A$

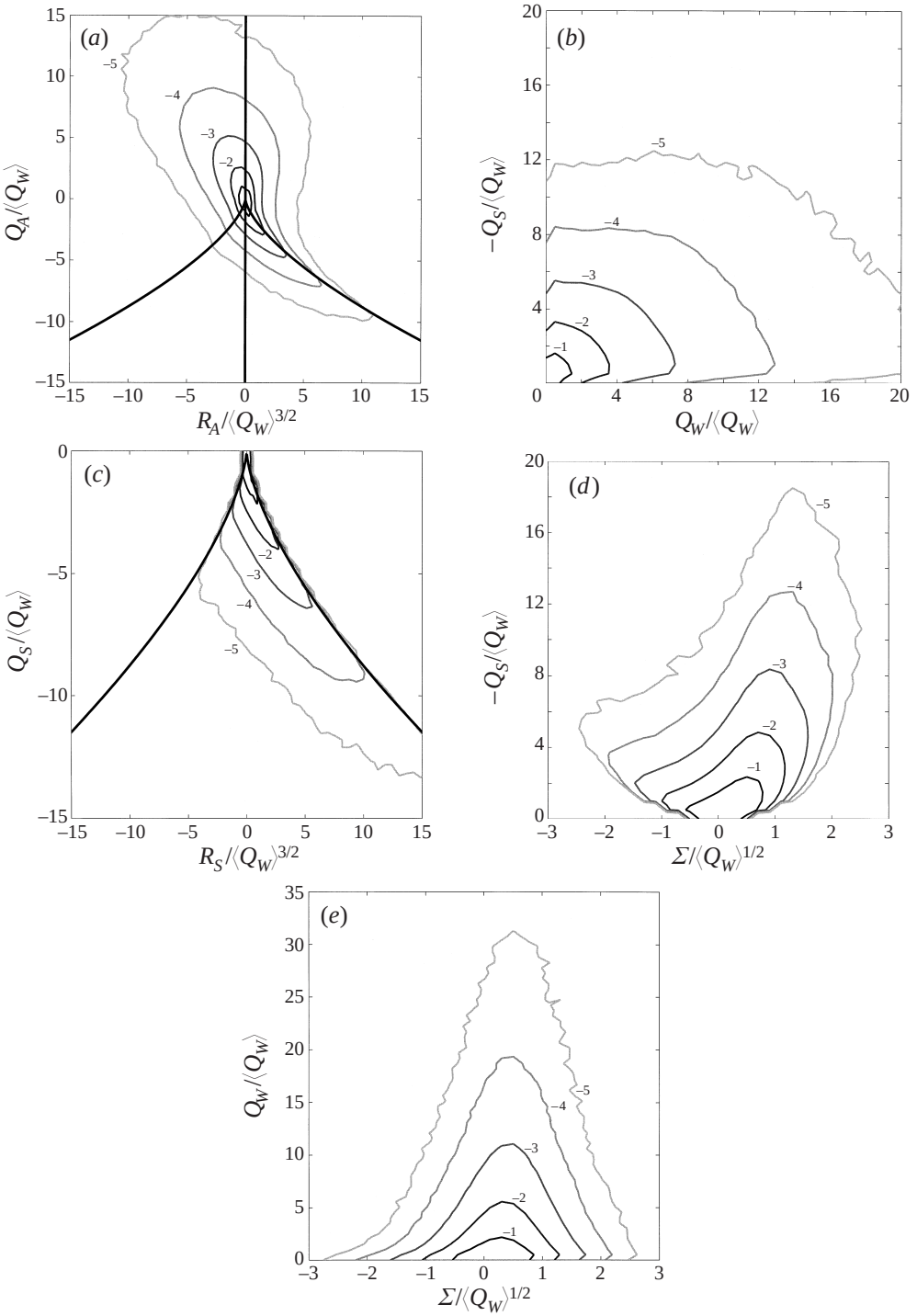

FIGURE 8. Joint PDF for simulation at $Re_\lambda = 70.9$ of (*a*) R_A vs. Q_A, (*b*) Q_W vs. $-Q_S$, (*c*) R_S vs. Q_S, (*d*) Σ vs. $-Q_S$, (*e*) Σ vs. Q_W. The difference between each contour level is one decade with darker shaded contour lines indicating higher region. The exponents of the decade level are indicated on the contour lines.

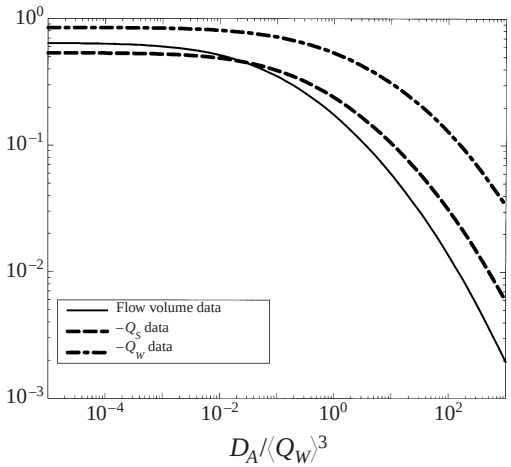

FIGURE 9. Normalized conditional volume-integrated data of: (i) flow volume; (ii) $-Q_S$; (iii) Q_W. The condition for the integration is that $D_A > D_A$ (*given*); the normalized D_A (*given*)$/\langle Q_W\rangle^3$ is the independent variable in this plot. The normalization factor for the conditional integrals is the respective unconditional integral over the entire flow volume.

(*given*) relative to the total flow volume; (ii) how much of the integrated $-Q_S$ is given by regions with $D_A > D_A$ (*given*); and (iii) how much of the integrated Q_W is given by regions with $D_A > D_A$ (*given*). These data show that regions with $D_A \geqslant 0$ account for approximately 64% of the total flow volume. As expected almost all of the integrated Q_W is found within the regions with $D_A \geqslant 0$, i.e. approximately 85%. What is perhaps surprising is that focal regions also account for more than half of the total dissipation of mechanical energy, i.e. focal regions contain approximately 54% of the integrated $-Q_S$. It is interesting to note that with respect to Q_W and $-Q_S$, there is little change in the integrals once $D_A \leqslant 10^{-2}\langle Q_W\rangle^3$. This suggests that most of the dynamically important focal motions in this flow volume have $D_A > 0.01\langle Q_W\rangle^3$ and these regions are also responsible for dissipating approximately 50% of the total kinetic energy.

The relationships of the conditional mean Q_W and $-Q_S$ as a function of D_A are shown in figure 10. This plot indicates that the relationship between the mean Q_W and D_A is approximated well by a 1/3 power law for $D_A/\langle Q_W\rangle^3 \geqslant 1$. This result can be deduced from (5) for large values of D_A, provided that the following conditions are satisfied:

$$\frac{Q_S}{Q_W} \ll 1$$

and

$$|R_A| \ll \left(\tfrac{4}{27}\, Q_W^3\right)^{1/2}.$$

The conditional mean dissipation of kinetic energy represented by $\langle -Q_S|D_A\rangle$ is also found to increase with D_A as shown in figure 10, but at a lower rate than $\langle Q_W|D_A\rangle$. The point to note here is that $\langle -Q_S|D_A\rangle$ follows a 1/7 power law quite accurately for the entire positive D_A range of values. The explanation for this result is not clear at this stage.

The focal structures in the flow are visualized in figure 11 using an iso-surface value of $D_A = 125\langle Q_W\rangle^3$. From the results presented in figure 10 it is deduced that these structures have a mean Q_W value of $6\langle Q_W\rangle$, which is equivalent to $\omega = 2.4\omega_{rms}$. Hence, these focal structures do not fall into the 'intense vorticity or worms' category

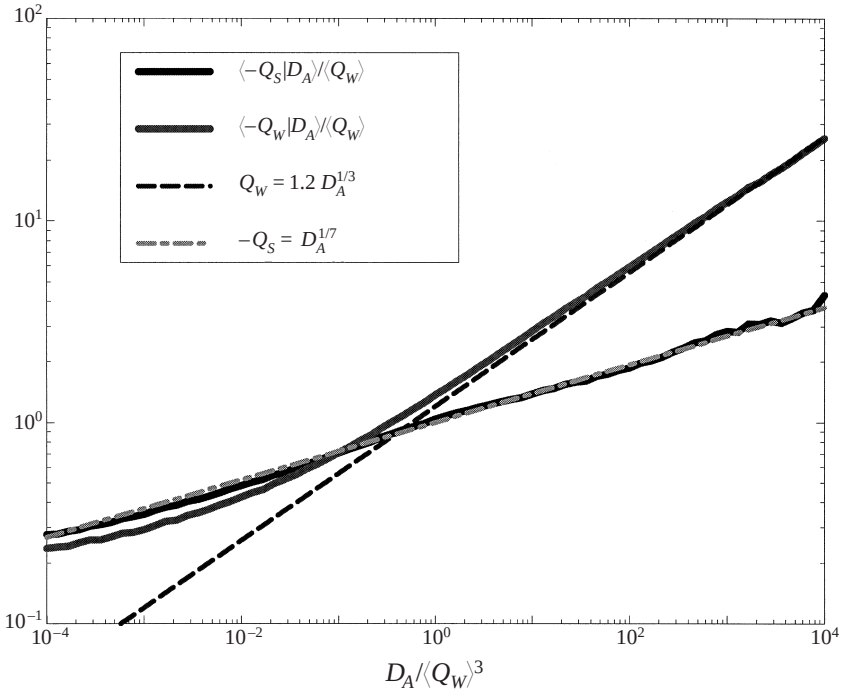

FIGURE 10. Normalized conditional average of Q_W and Q_S for positive D_A.

of Jiménez *et al.* (1993), but as can be clearly observed from the visualization in figure 11 they form quite distinct and compact coherent structures (or worms) .

The topological classification of the flow provides additional geometric information on the structure of these *worms* which are only composed of focal regions and henceforth will be referred to as *focal structures.* The SF/S regions of the focal structures are in general elongated and compact and occupy most of the focal volume. The UF/C regions resemble 'blobs' and are found: (i) predominantly at one of the ends of the focal structures; (ii) in regions where the focal structure bends; or (iii) in focal regions joining two regions of SF/S topology. Reducing the iso-surface D_A level appears to increase the cross-sectional size of the SF/S regions and the *blobbiness* of the UF/C regions, but not the general structure.

5.2. *Conditional mean time rate of change of invariant vector fields and mean trajectories*

The joint PDFs presented in the previous section only give a static instantaneous picture of the correlation between different invariant quantities. On the other hand, the conditional mean time rate of change of the invariant vector fields and the CMT introduced in §4 give a representation of the mean Lagrangian evolution of these invariants, albeit only as a conditional mean. In this section the conditional mean time rate of change of the invariants of A_{ij}, S_{ij} and W_{ij} and their corresponding CMT in their two-dimensional invariant phase planes are presented.

To illustrate the dynamical effects of H_{ij}, the CMT are calculated with and without H_{ij} contributions. In order to ensure that the CMT computed in this section are not dependent on the random forcing at the large scales, similar plots have been produced and analysed for the case of decaying isotropic turbulence. Qualitatively, the CMT

computed from these data are similar to the plots shown here for forced isotropic turbulence. Hence, all discussion in this section is independent of the large-scale forcing scheme used to sustain the turbulence.

5.2.1. *The* (R_A, Q_A) *phase plane*

Figure 12 shows the conditional mean vector field $(\dot{Q}_A(R_A, Q_A), \dot{R}_A(R_A, Q_A))$, in the (R_A, Q_A) invariant phase plane. In the neighbourhood of the origin along the null discriminant curve for $R_A > 0$, all vectors have very small magnitude. This suggests that the mean time rates of change of Q_A and R_A are quite small in flow regions which have small gradients (i.e. in regions with small D_A values). It is clearly observable that the directions of the mean vectors in the (R_A, Q_A) phase plane where $R_A/\langle Q_W \rangle^{3/2} > 5$ and $D_A < 0$ are not well defined, whereas the directions of the $(\dot{Q}_A(R_A, Q_A), \dot{R}_A(R_A, Q_A)$ vectors are well defined for $D_A > 0$ and where the value of the corresponding joint PDF is greater than 10^{-4}. The CMT in this invariant phase plane are therefore only calculated in regions where the mean vectors are well defined.

Figure 13(*a*) shows the CMT in the (R_A, Q_A) invariant phase plane. The trajectories move in a clockwise fashion spiralling towards the origin. This indicates that in the mean, the local topology of fluid particles will change in a cyclical manner from UN/S/S to SN/S/S to SF/S to UF/C. Trajectories started with high values of Q_A and R_A go through the same sequence of topological evolution (UN/S/S $\rightarrow$ SN/S/S $\rightarrow$ SF/S $\rightarrow$ UF/C) a few times before finally spiralling into the origin. This is in stark contrast to the trajectories predicted using the restricted Euler model (see Cantwell 1992).

Since decreasing values of Q_A and R_A imply decreasing values of velocity gradients, this observation suggests that in the mean, fluid particles move from regions dominated by small-scale motions to regions where the large-scale motion is dominant. Some evidence that the CMT are representative of *actual* Lagrangian trajectories in the (R_A, Q_A) phase plane was provided in a study of wall-bounded flows by Chong *et al.* (1998), where it was shown that fluid particles with initial local topology SF/S will generally evolve towards the origin of the (R_A, Q_A) invariant phase plane, while the local topology changes from SF/S to UF/C.

Since the CMT have this clockwise spiralling motion which crosses the $D_A = 0$ curve several times, Martin *et al.* (1998) hypothesized that this spiralling motion might be periodic. Their investigation showed that the cyclical evolution in the (R_A, Q_A) phase plane has a repeatable period equal to $T_0 \approx 30t_\eta = 3\tau_{eddy}$, where t_η is the Kolmogorov time scale and τ_{eddy} is the eddy turnover time. It is worth noting that T_0 compares well with the Lagrangian integral time scale estimated by Corrsin (1963).

Conditional mean trajectories in the (R_A, Q_A) phase plane have also been calculated assuming $H_{ij} = 0$ to investigate its effect on the conditional evolution. These CMT are shown in figure 13(*b*). Integration was only carried out where the mean vector field is well defined. Comparing figure 13(*a*) with figure 13(*b*) shows that in regions where the local topology is UF/C, terms involving H_{ij} have a dissipative role. The CMT in these regions have a tendency to go towards the origin of the (R_A, Q_A) phase plane. In regions where $D_A < 0$, figure 13(*b*) shows that the CMT go from left to right whereas figure 13(*a*) shows the CMT going from right to left. Hence, the terms involving the H_{ij} tensor alters the sign of $\mathrm{D}R_A/\mathrm{D}t$ in non-focal regions of the flow field and thus has a marked effect on the evolution of the invariant.

Figure 14 shows vortex lines which are coloured according to the local topology demonstrating that regions where the vortex lines are well-organized have SF/S topology, while regions which are not so well organized have a UF/C type of local

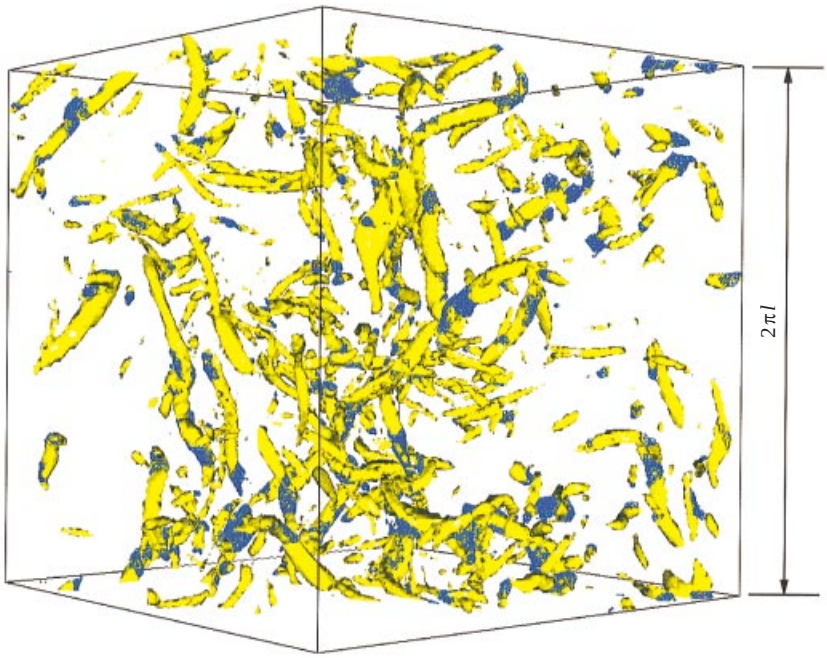

FIGURE 11. Iso-surface of the discriminant, D_A, used to visualize focal structures. The yellow iso-surface represents flow regions with SF/S topology while the blue outlines of the iso-surface show UF/C topology flow regions. The iso-surfaces of both SF/S and UF/C correspond to $D_A = 125\langle Q_W\rangle^3$ and the entire flow domain of the 128^3 simulation at $Re_\lambda = 70.9$ is shown.

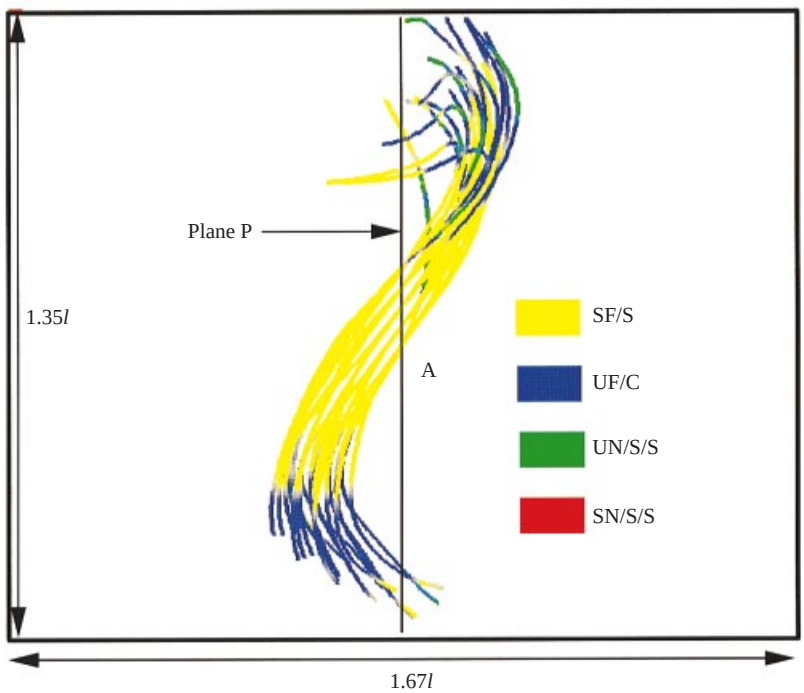

FIGURE 14. Vortex lines through a plane (coloured in white) of the flow field where the value of $Q_W/\langle Q_W\rangle$ is high for DNS at $Re_\lambda = 70.9$. The vortex lines are coloured according to the local topology.

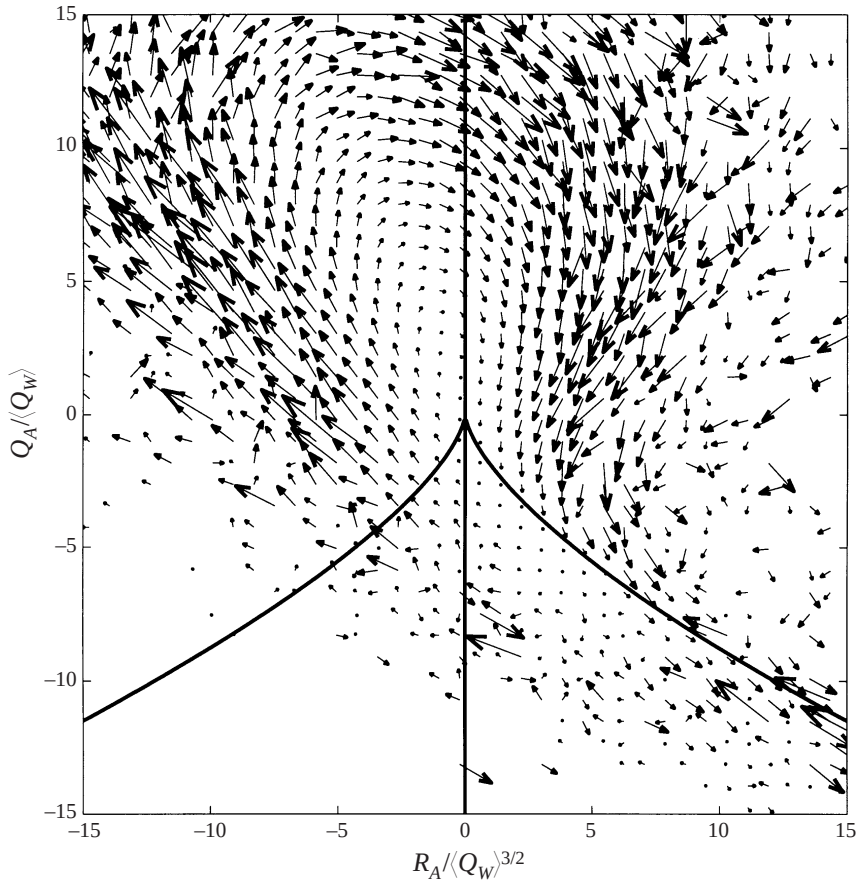

FIGURE 12. Conditional mean vectors of $\dot{Q}_A$ and $\dot{R}_A$ computed from data of forced isotropic turbulence at $Re_\lambda = 70.9$.

topology. This is also clearly shown in figure 11 where the yellow iso-surfaces of D_A represent regions with SF/S topology while the blue iso-surfaces represent regions with UF/C topology.

Figure 15 shows the detailed focal structure in a quarter of the total flow volume. Figure 15(a, b) shows yellow SF/S vorticity vectors with $D_A/\langle Q_W\rangle^3 \geqslant 100$ and blue UF/C vorticity vectors with $D_A/\langle Q_W\rangle^3 \geqslant 50$. Vortex lines through a single focal structure have been included to show their compact form and well organized nature in SF/S regions. The vortex lines have a tendency to diverge in UF/C regions. Figure 15(c, d) shows corresponding SF/S surfaces with an iso-level of $D_A/\langle Q_W\rangle^3 = 300$ and UF/C surfaces with and iso-level of $D_A/\langle Q_W\rangle^3 = 20$; these iso-surfaces have been drawn with some transparency to show where the vortex lines lie inside or outside the focal structure. Figure 15(e) shows that the SF/S component of a focal structure is predominantly compact and elongated, while figure 15(f) shows that UF/C regions envelop the SF/S structure like a sleeve or are predominantly *blobby* in nature and located at the tip of well-defined tubular SF/S regions or in focal regions containing kinks or bends.

A scenario for the mean evolution of fluid particles can be conjectured from the behaviour of the CMT in relation to the focal structures in the flow field. A particle

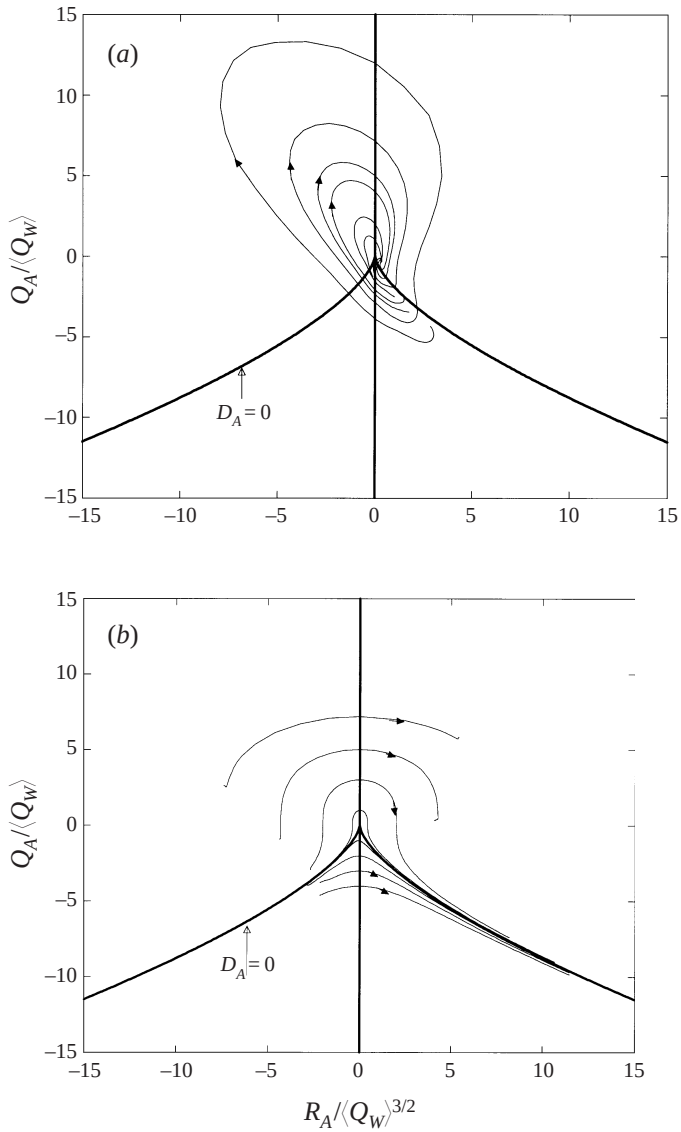

FIGURE 13. Conditional mean trajectories of the invariants Q_A and R_A computed using (*a*) data of forced isotropic turbulence at $Re_\lambda = 70.9$, and (*b*) data of homogeneous isotropic turbulence assuming $H_{ij} = 0$.

in the vicinity of a coherent SF/S structure, in a location just outside the *core* of the coherent structure where the local topology is probably UN/S/S, will be sucked into the core of the structure which is essentially a low-pressure region. The local topology (as seen by an observer moving with the particle) changes from UN/S/S via SN/S/S to SF/S. The particle then moves along the core of the structures to regions where the focal structure loses its compact nature due to contraction of the focal structure and the local topology changes to UF/C. Contraction of the focal structure leads to a decrease in the magnitude of the velocity gradients and thus a decrease in the local values of Q_A and R_A and hence the spiralling of the CMT in the (R_A, Q_A) phase space towards the origin.

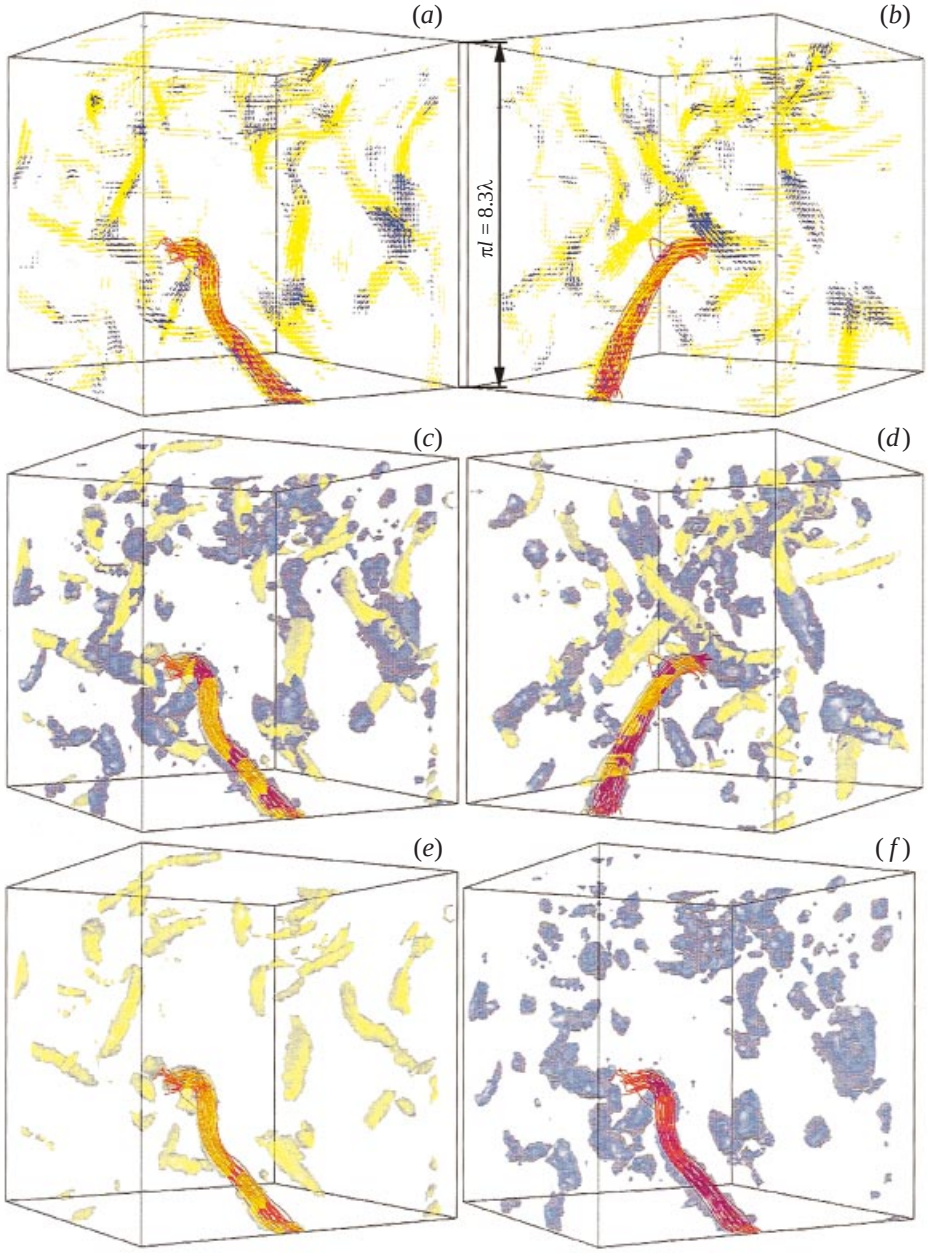

FIGURE 15. Conditional vorticity vector fields and iso-contours of D_A for SF/S and UF/C flow topologies for 0.25 of the computed flow domain. Vortex lines through the core of a SF/S region containing the highest values of D_A are also indicated. (a, b) Different views of the conditional vorticity vector field: the yellow vectors indicate SF/S regions with $D_A \geqslant 100\langle Q_W\rangle^3$, whereas the blue vectors indicate UF/C regions with $D_A \geqslant 50\langle Q_W\rangle^3$; the red vortex lines are only computed for one of the dominant structures in this flow region. (c, d) The corresponding views of (a) and (b) with the focal structures identified using correspondingly coloured iso-surfaces of D_A: the SF/S iso-surface is shown for $D_A \geqslant 300\langle Q_W\rangle^3$ while the UF/C iso-surfaces are shown for $D_A \geqslant 20\langle Q_W\rangle^3$; the iso-surfaces have been drawn with transparency to show where the vortex lines lie inside these focal structures. (e,f) The same iso-surfaces as (a) and (b) with (e) only showing the SF/S structures and (f) only showing the UF/C structures. The vortex lines are shown for the same region in all the focal visualizations.

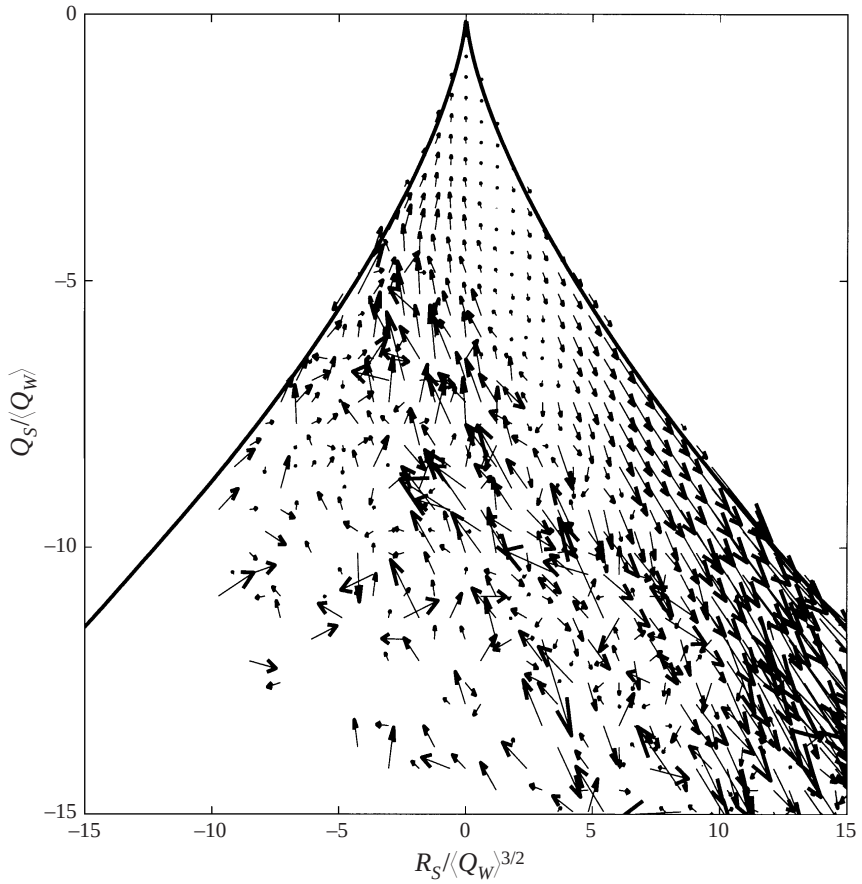

FIGURE 16. Conditional mean time rate of change vectors of R_S and Q_S computed using data of forced isotropic turbulence at $Re_\lambda = 70.9$.

This is a very simplistic interpretation which only applies in the mean. It is at this point worth recalling that the conditional averaging has masked the fine detail of the topological evolution of individual fluid particles and replaced it with the average evolution of an ensemble of many particles all of which started with the same initial value for R_A and Q_A.

5.2.2. *The* (R_S, Q_S) *phase plane*

Conditional mean vectors in the (R_S, Q_S) phase plane are shown in figure 16. Similarly to the (R_A, Q_A) phase plane, the magnitude of the vectors close to the origin is smaller than the magnitude of the vectors away from the origin indicating that the magnitude of $\dot{R}_S(R_S, Q_S)$ and $\dot{Q}_S(R_S, Q_S)$ is small when the magnitude of both R_S and Q_S is small. Figure 17 shows the CMT emerging from what appears to be an unstable focus in the (R_S, Q_S) phase plane. Some of the CMT go towards the origin and some of them diverge to regions with large values of R_S and $-Q_S$. The location of the unstable focus is more clearly illustrated in figure 18(*a*) which shows an enlarged view close to the origin in the (R_S, Q_S) phase plane. The location of the unstable focus is shown to be at approximately $(R_S/\langle Q_W\rangle^{3/2}, Q_S/\langle Q_W\rangle) \simeq (1, -2)$ for the data at $Re_\lambda = 48.2$. A corresponding close up view of the unstable focus computed using the

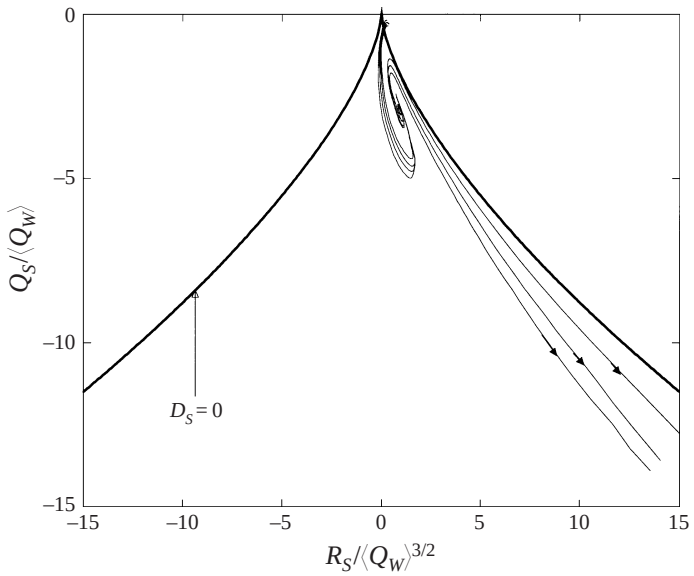

FIGURE 17. The CMT of the invariants R_S and Q_S computed from data of forced isotropic turbulence at $Re_\lambda = 70.9$ corresponding to vector field shown in figure 16.

$Re_\lambda = 70.9$ simulation data is shown in figure 18(b) where the location of the unstable focus is shown to be at $(R_S/\langle Q_W \rangle^{3/2}, Q_S/\langle Q_W \rangle) \simeq (1, -3)$, indicating that there may be a trend for the location of this unstable focus to move to larger $-Q_S/\langle Q_W \rangle$ values at higher Re_λ.

Closer observation of figure 18 reveals that some of the trajectories close to the origin of the (R_S, Q_S) phase plane appear to go above the $D_S = 0$ line. This error was traced to the discrete nature and finite resolution used to represent the conditional mean vector fields. CMT computed with smaller bins allow all trajectories to head exactly to the origin of this plane, but statistical convergence in the computations of the conditional mean time rate of change of R_S and Q_S is then not guaranteed for large values of R_S and Q_S.

The effect of the terms containing the H_{ij} tensor was also investigated by calculating the corresponding CMT with $H_{ij} = 0$. These results are shown in figure 19. The CMT in this figure travel from left to right in the (R_S, Q_S) phase plane. For large values of $-Q_S$, the CMT are similar to the CMT in figure 17 indicating that the terms involving H_{ij} have a negligible effect on the CMT structure and hence the mean evolution of R_S and Q_S for large values of $-Q_S$. However, for small values of $-Q_S$ the terms involving H_{ij} are important and have the effect of dragging the CMT towards the origin of the (R_S, Q_S) phase plane.

5.2.3. *The* $(Q_W, -Q_S)$ *phase plane*

Figure 20 shows the conditional mean time rate of change vector field in the $(Q_W, -Q_S)$ phase plane. Vectors close to the origin are small, indicating that $\dot{Q}_W(Q_W, -Q_S)$ and $-\dot{Q}_S(Q_W, -Q_S)$ have small values. The corresponding CMT plot is shown in figure 21(a), illustrating that some trajectories start with low Q_W and low to moderate values of $-Q_S$ and move to regions dominated by rotational motions (high value of $\mathscr{K}$) at slightly increasing levels of $-Q_S$. These trajectories are found to then return to the origin via regions with lower values of $-Q_S$. There are also trajectories

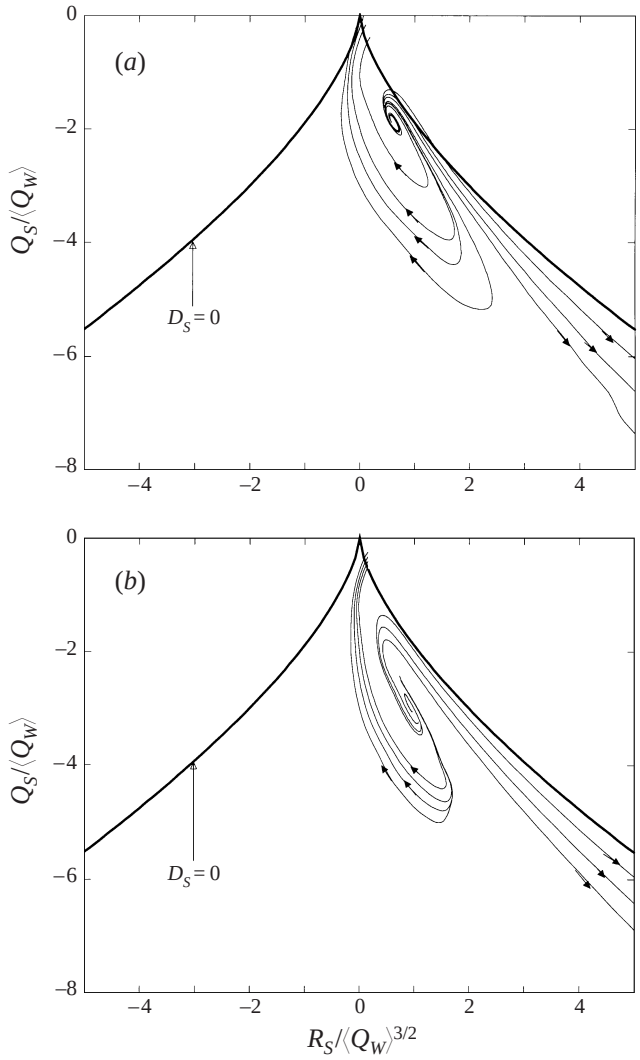

FIGURE 18. A closer view of the unstable focus closer to the origin in the (R_S, Q_S) phase plane for (*a*) $Re_\lambda = 48.2$, and (*b*) $Re_\lambda = 70.9$.

that appear to move simultaneously to large values of Q_W and $-Q_S$ and this is especially evident in regions where $\mathscr{K}$ is small. An interesting observation is that for small values of $\mathscr{K}$, $-\dot{Q}_S(Q_W, -Q_S)$ is found to be positive indicating an increase in the mean value of $-Q_S$. In contrast, regions with large values of $\mathscr{K}$ have negative values of $\dot{Q}_W(Q_W, -Q_S)$, indicating that there is a decrease in the mean value of Q_W.

Conditional mean trajectories have also been computed assuming that $H_{ij} = 0$ and these are shown in figure 21(*b*). The CMT in regions where Q_W is low have the same trends as those found in figure 21(*a*) indicating that in these regions the effect of the terms involving H_{ij} is not so important in the mean evolution of Q_W and $-Q_S$. However, the CMT in figures 21(*a*) and 21(*b*) look quite different in regions where $\mathscr{K}$ is high. Hence, terms involving H_{ij} play an important role here. By comparing

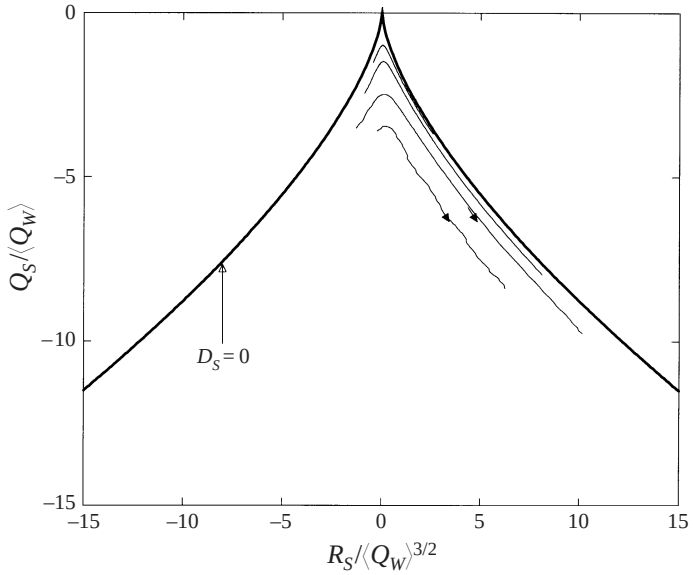

FIGURE 19. The CMT of the invariants R_S and Q_S computed using data of forced isotropic turbulence at $Re_\lambda = 48.2$ assuming that $H_{ij} = 0$.

figure 21(a) with 21(b) it is easily seen that the mean effects of the terms involving H_{ij} at high values of $\mathscr{K}$ is to force the CMT to go towards the origin of the (Q_W, $-Q_S$) phase plane.

5.2.4. *The* (Σ, Q_W) *phase plane*

The CMT in the (Σ, Q_W) phase plane are shown in figure 22(a). Figure 22(b) is a closer view of the CMT in the neighbourhood of the origin of the (Σ, Q_W) phase plane. The trajectories travel in an anti-clockwise fashion, indicating that positive values of Σ are correlated with increasing values of Q_W and negative values of Σ are correlated with decreasing values of Q_W. This is expected because the local stretching of enstrophy is associated with positive values of Σ whereas the contracting of enstrophy is associated with negative values of Σ. Trajectories closer to the origin will spiral into the point $(\Sigma/\langle Q_W\rangle^{1/2}, Q_W/\langle Q_W\rangle) \simeq (0.25, 0.75)$. Trajectories that are started further away from the origin travel in an anti-clockwise direction to high values of Q_W, reaching a maximum Q_W. Viscous diffusion and vorticity contraction effects subsequently reduce Q_W to a small and possibly zero value.

Some further interesting results can be deduced from the conditional evolution of Q_W and Σ shown in figure 22 by reference to the governing equation for Q_W,

$$\begin{aligned}\frac{\mathrm{D}Q_W}{\mathrm{D}t} &= 2\Sigma\, Q_W + \tfrac{1}{2}\nu\omega_i\frac{\partial^2\omega_i}{\partial x_j\partial x_j}\\ &= 2\Sigma\, Q_W - W_{ik}H^W_{ki}\\ &= 2\Sigma\, Q_W + \nu\frac{\partial^2 Q_W}{\partial x_j\partial x_j} - \tfrac{1}{2}\nu\frac{\partial\omega_i}{\partial x_j}\frac{\partial\omega_i}{\partial x_j}.\end{aligned} \tag{34}$$

The available data suggest that Q_W becomes zero as shown in figure 22. However,

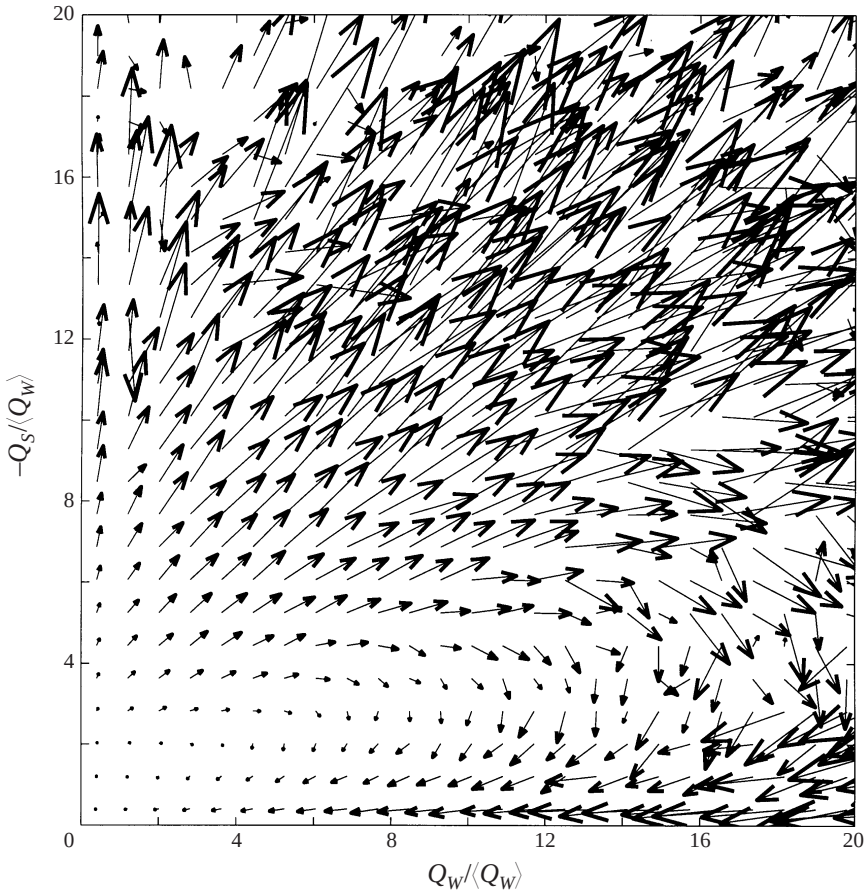

FIGURE 20. Conditional mean time rate of change vectors of $-Q_S$ and Q_W computed using data of forced isotropic turbulence at $Re_\lambda = 70.9$.

this effect could be due to the finite number of data bins in the (Σ, Q_W) phase plane. Any conditional mean increase in Q_W requires a non-zero Q_W as indicated by (34), and since figure 22(*b*) indicates what appears to be an increase of Q_W from a zero base, one is led to the conclusion that Q_W decreases for $\Sigma < 0$ in the mean to a small but non-zero value and keeps on decreasing while Σ starts to increase again turning from vorticity contraction to vorticity stretching.

The CMT in figure 22(*b*) show that for small values of Q_W and for $\Sigma > 0$ there is a conditional mean increase in Q_W due to vortex stretching with the conditional mean time rate of change of Σ always negative for $Q_W/\langle Q_W\rangle \geqslant 1$. Following a given CMT for $\Sigma > 0$ from $Q_W/\langle Q_W\rangle \approx 0$, the maximum value of Σ is always attained when $\dot{\Sigma} = 0$. As is evident from figure 22(*b*), $Q_W/\langle Q_W\rangle \approx 0.7$ whenever $\dot{\Sigma} \approx 0$.

In a similar fashion the maximum Q_W value following a given trajectory is reached when $\dot{Q}_W$ is zero. At this point (34) indicates that there is an exact balance between the conditional mean vorticity stretching and viscous diffusion effects. These maxima in Q_W for the CMT shown in figure 22(*b*) are always found to occur for $\Sigma > 0$. This result indicates that the initial decrease in Q_W, once it has reached a maximum

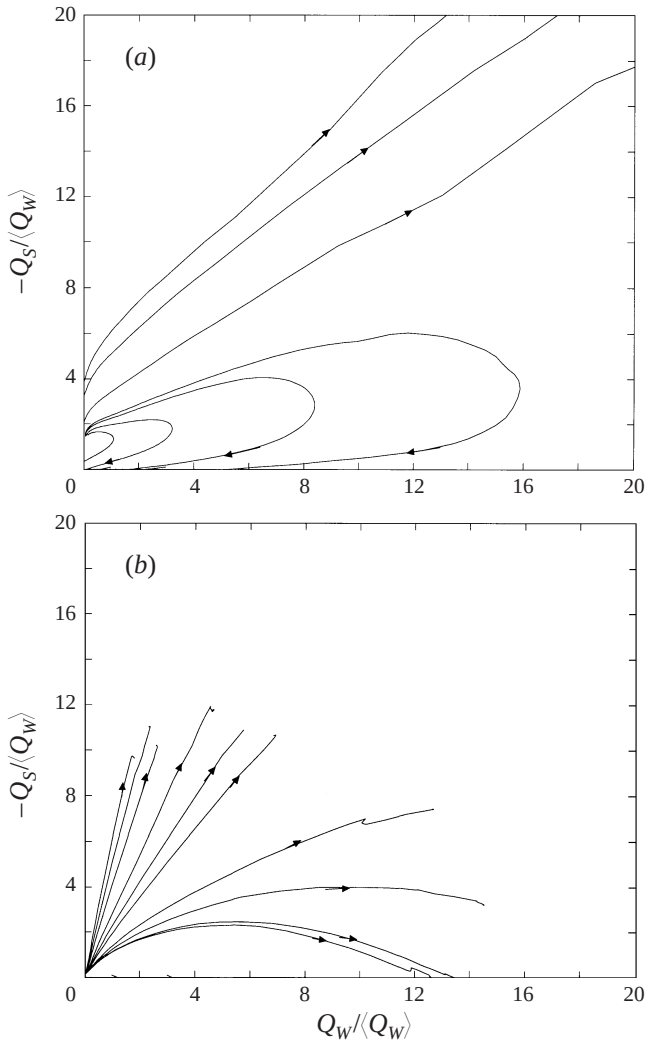

FIGURE 21. (*a*) The CMT of the invariants Q_W and $-Q_S$ computed from data of forced isotropic turbulence at $Re_\lambda = 70.9$ shown in figure 20. (*b*) The corresponding CMT of the invariants Q_W and $-Q_S$ computed from data of forced isotropic turbulence at $Re_\lambda = 48.2$ and assuming that $H_{ij} = 0$.

value, is not due to vorticity contraction, but rather to viscous diffusion effects. This point is clearly illustrated in both figures 22(*a*) and 22(*b*) by the fact that $\dot{Q}_W < 0$ and $\Sigma > 0$ after the maximum Q_W value is reached, which by reference to (34) implies that viscous effects must dominate over the vorticity stretching effect in this region of the trajectory evolution. Once the trajectories cross the $\Sigma = 0$ line, then both vorticity contraction and viscous diffusion act together to reduce Q_W further.

The maximum vorticity contraction rate is found to occur when $\dot{\Sigma} = 0$. The CMT shown in figure 22(*b*) suggest that in this region the strain field changes in such a way as to reduce vorticity contraction and ultimately reach a state where vorticity stretching is again present. During this evolution of the strain field, Q_W is found to continually decrease, albeit at a very small rate. This decrease of Q_W along

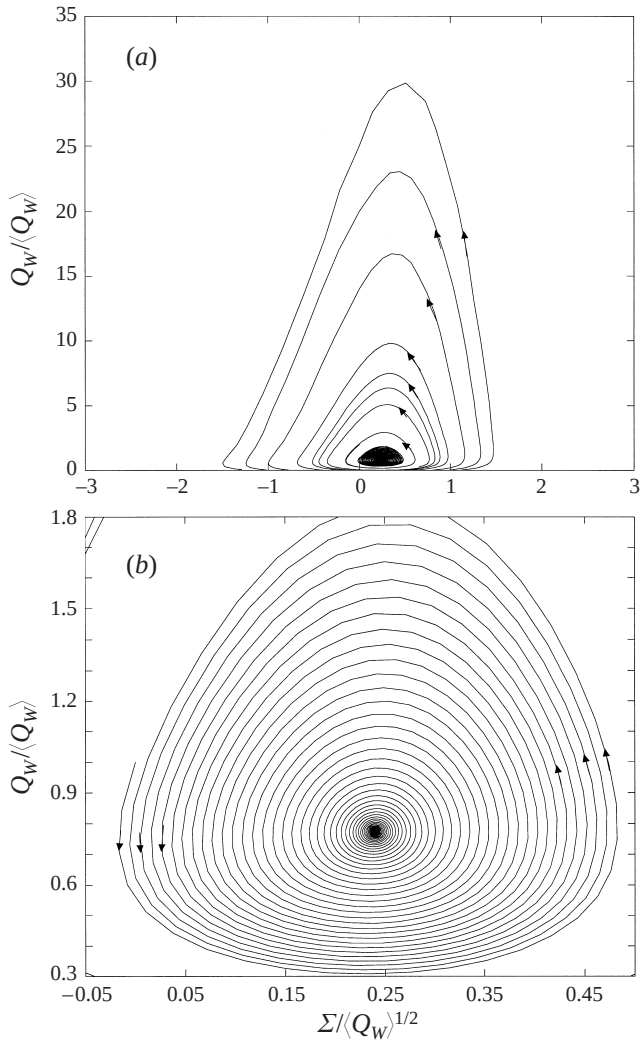

FIGURE 22. (*a*) The CMT of the invariants Σ and Q_W computed from data of forced isotropic turbulence at $Re_\lambda = 70.9$. (*b*) A magnified view of the stable focus located at approximately $(\Sigma/\langle Q_W\rangle^{1/2}, Q_W/\langle Q_W\rangle) = (0.25, 0.7)$.

a CMT is found to persist even though vorticity stretching is again present. This negative conditional mean time rate of change of Q_W continues until a threshold value of vorticity stretching represented by $\Sigma/\langle Q_W\rangle^{1/2} \approx 0.25$ is reached. Only then does one observe that $\dot{Q}_W$ changes sign and Q_W begins to increase again along a CMT. This effect is shown clearly in figure 23, where the conditional mean rate of change of Q_W has been computed for the appropriate range of normalized stretching rates. The zero conditional mean rate of change of Q_W is found to be given when $\Sigma \approx 0.25\,\langle Q_W\rangle^{1/2}$.

The cyclical nature of the CMT in the (Σ, Q_W) phase plane has also been investigated in some detail. The evolution of $\dot{Q}_W$ and $\dot{\Sigma}$ in this phase plane is found to be self-similar if normalized by the maximum value attained during each cycle. Figure 24

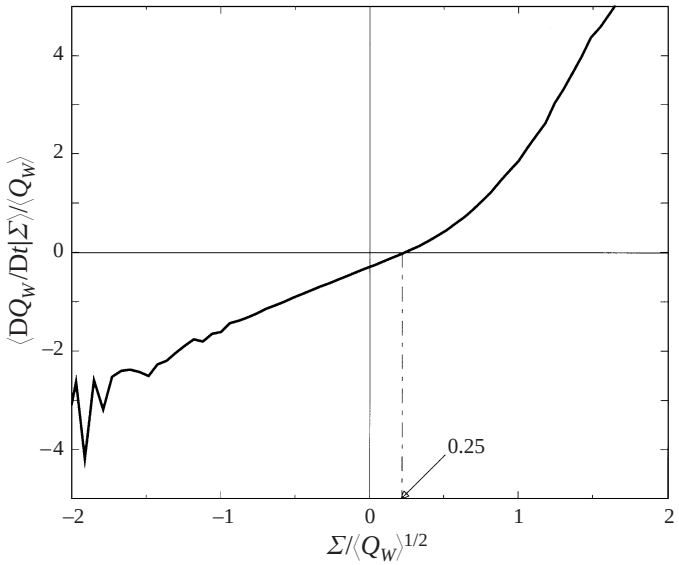

FIGURE 23. Normalized conditional mean rate of change of Q_W, $\langle DQ_W/Dt|\Sigma\rangle / \langle Q_W\rangle$, as a function of the normalized rate of stretching, $\Sigma/\langle Q_W\rangle^{1/2}$.

shows this result for $\dot{Q}_W/\langle Q_W\rangle^{3/2}$, where $\dot{Q}_W/\langle Q_W\rangle^{3/2}$ normalized by its maximum value during a cycle has been plotted for a number of evolution cycles. The results for $\dot{\Sigma}$ are similar. The cycle period is found to be slightly larger than that found by Martin *et al.* (1998) for the (R_A, Q_A) phase plane, i.e. $T_0^* \approx 1.15T_0$, where T_0^* represents the period deduced from the data in the (Σ, Q_W) phase plane. It is interesting to note that in the (Σ, Q_W) conditional phase plane a limit cycle behaviour is also present. Data in the domain $0.21\langle Q_W\rangle < Q_W < 2.25\langle Q_W\rangle$ and $-0.07\langle Q_W\rangle^{1/2} < \Sigma < 0.54\langle Q_W\rangle^{1/2}$ spiral into the point located at approximately (0.25, 0.75), while data outside this domain spiral outwards away from this point.

The data shown in figure 22(*a*) are consistent with the idea of a stretched vortex. Positive values of Σ are associated with focal coherent structures that are being stretched where fluid particles are attracted to the low-pressure region at the core of the focal structure. As fluid particles approach the focal core, the local value of Q_W increases. Negative values of Σ are associated with focal coherent structures that are being contracted and hence have a local UF/C topology. This topological behaviour tends to be observed towards the tips of focal structures as shown in the iso-discriminant visualization in figure 11 the vortex line visualization of figure 14 and as previously reported in the topological visualizations of focal structures in turbulent mixing layers and wakes by Soria & Cantwell (1994). At the extremities of these focal structures the fluid particles are being forced away from the core due to vorticity contraction. As UF/C fluid regions move away from the core of these focal structures, the local value of Q_W is found to decrease.

5.2.5. *The* $(\Sigma, -Q_S)$ *phase plane*

Figure 25(*a*) shows the CMT in the $(\Sigma, -Q_S)$ phase plane with a magnified view of the region close to the origin shown in figure 25(*b*). It is observed that some of the trajectories travel in a clockwise manner towards a region where $(\Sigma/\langle Q_W\rangle^{1/2}, -Q_S/\langle Q_W\rangle) \simeq (-0.15, 0.2)$. The clockwise orientation of the $(\Sigma, -Q_S)$ system is

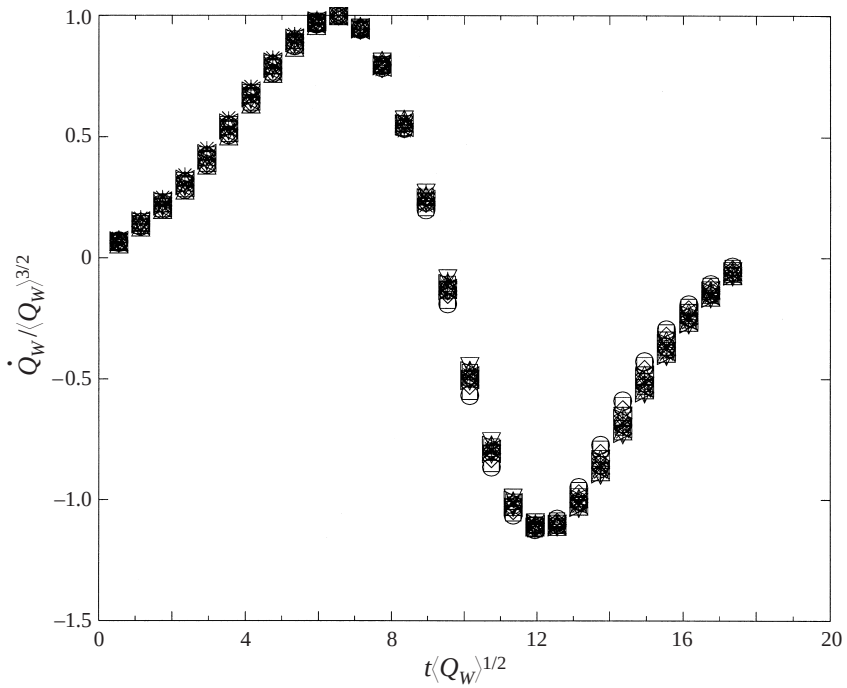

FIGURE 24. Evolution of $\dot{Q}_W/\langle Q_W\rangle^{3/2}$ for a number of cycles. The dependent data for each cycle have been normalized by its maximum value during the cycle.

contrary to the anti-clockwise orientation of the (Σ, Q_W) system. Clockwise trajectories in the $(\Sigma, -Q_S)$ system indicate that decreasing values of $-Q_S$ are associated with positive values of Σ, i.e. vorticity stretching, while increasing values of $-Q_S$ are associated with negative values of Σ, i.e. vorticity contraction. Note that the stable node in this system is located at a negative value of Σ, whereas for the (Σ, Q_W) system the location of the stable node is at a positive value of Σ. CMT in regions where the value of $-Q_S$ is large appear to move to even larger values of $-Q_S$. However, the joint PDF shown in figure 8(*d*) indicates that the probability of fluid evolving along these latter CMT is very rare.

6. Conclusions

Computations of homogeneous isotropic turbulence are used in this study to investigate focal regions which are defined as regions where D_A is greater than a small positive value (i.e. $D_A \geqslant 0.01\,\langle Q_W\rangle^3$). These regions occupy 64% of the fluid volume and contain 85% of the integrated Q_W (or enstrophy) and 54% of the total dissipation of mechanical energy. The data also show that $\langle Q_W|D_A\rangle \propto D_A^{1/3}$ for $D_A \geqslant 1\,\langle Q_W\rangle^3$, i.e. when $Q_S/Q_W \ll 1$ and $|R_A| \ll \left(\frac{4}{27}\,Q_W^3\right)^{1/2}$, as expected from the theoretical analysis. However, the data also show that $\langle -Q_S|D_A\rangle \propto D_A^{1/7}$ for $D_A \geqslant 0$, an unexpected result which may warrant further investigation.

The idea of using conditional averages to obtain mean time rate of change of invariants and trajectories in the phase planes of invariants is novel and provides significant new information on the dynamics of the invariants. Evolution character-

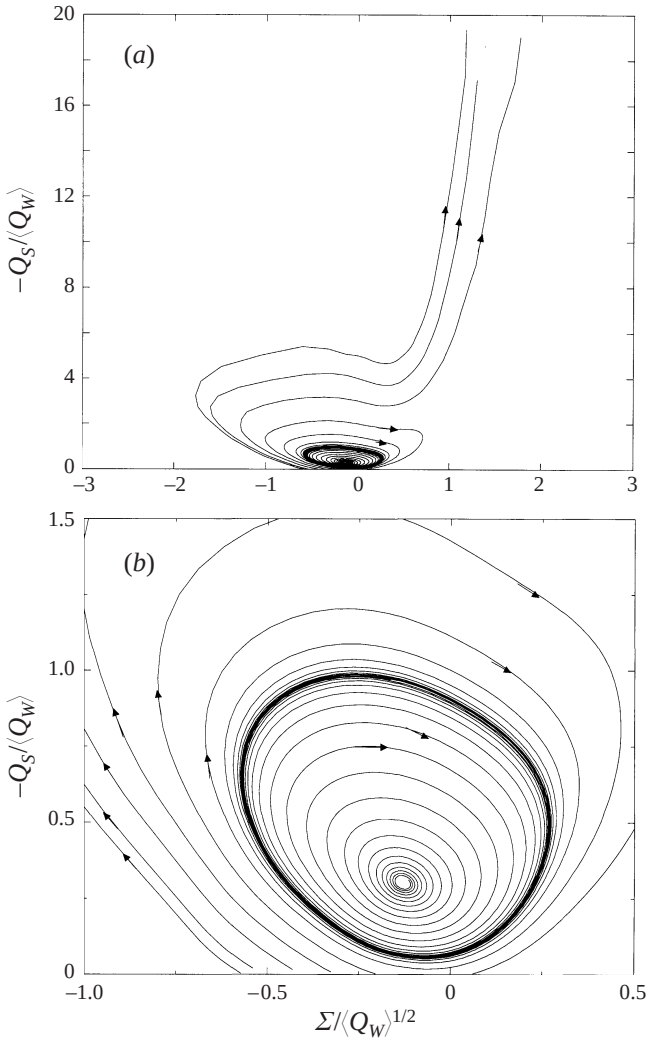

FIGURE 25. (*a*) The CMT of the invariants Σ and $-Q_S$ computed from data of forced isotropic turbulence at $Re_\lambda = 70.9$. (*b*) A magnified view of the origin.

istics are shown in terms of trajectories in the various phase planes of invariants. These trajectories are the 'line-of-sight' average onto a two-dimensional phase plane of complicated multi-dimensional dynamics.

This research was supported by a grant from the Australian Research Council which is gratefully acknowledged. J.M. also gratefully acknowledges the support of the Ministry of Science and Education of the Spanish Government by supporting this work through a fellowship.

REFERENCES

ASHURST, W., KERSTEIN, A., KERR, R. & GIBSON, C. 1987 Alignment of vorticity and scalar gradient with strain rate in simulated Navier–Stokes turbulence. *Phys. Fluids* **25**, 2343–2353.

BATCHELOR, G. 1960 *The Theory of Homogeneous Turbulence*. Cambridge University Press.

Blackburn, H. M., Mansour, N. N. & Cantwell, B. J. 1996 Topology of fine-scale motions in turbulent channel flow. *J. Fluid Mech.* **310**, 269–292.

Cantwell, B. J. 1992 Exact solution of a restricted Euler equation for the velocity gradient tensor. *Phys. Fluids* **4**, 782–793.

Chen, J., Chong, M. S., Soria, J., Sondergaard, R., Perry, A. E., Rogers, M., Moser, R. & Cantwell, B. J. 1990 A study of the topology of dissipating motions in direct numerical simulations of time-developing compressible and incompressible mixing layers. In *Proc. Summer Program 1990*. Centre for Turbulence Research, Stanford University.

Cheng, W. 1996 Study of the velocity gradient tensor in turbulent flow. PhD thesis. Stanford University. SUDAAR 685.

Chong, M., Perry, A. & Cantwell, B. 1990 A general classification of three-dimensional flow fields. *Phys. Fluids* **2**, 765–777.

Chong, M., Soria, J., Perry, A., Chacin, J., Cantwell, B. J. & Na, Y. 1998 A study of the tubulence structures of wall-bounded shear flows using dns data. *J. Fluid Mech.* **357**, 225–248.

Corrsin, S. 1963 Estimates of the relations between Eulerian and Lagrangian scales in large Reynolds number turbulence. *J. Atmos. Sci.* **20**, 115–119.

Dopazo, C., Valiño, L. & Martin, J. 1993 Velocity gradients in turbulent flows. Stochastic models. In *Proc. 9th Symp. on Turbulent Shear Flows, Kyoto, Japan.*

Eswaran, V. & Pope, S. 1988 An examination of forcing in direct numerical simulations of turbulence. *Computers Fluids* **16**, 257–278.

Girimaji, S. & Pope, S. 1990*a* A diffusion model for velocity gradients in turbulence. *Phys. Fluids* **2**, 242–256.

Girimaji, S. & Pope, S. 1990*b* Material-element deformation in isotropic turbulence. *J. Fluid Mech.* **220**, 427–458.

Girimaji, S. & Speziale, C. 1995 A modified restricted Euler equation for turbulent flows with mean velocity gradients. *Phys. Fluids* **7**, 1438–1446.

Jiménez, J., Wray, A., Saffman, P. & Rogallo, R. 1993 The structure of intense vorticity in isotropic turbulence. *J. Fluid Mech.* **255**, 65–90.

Kerr, R. 1987 Histograms of helicity and strain in numerical turbulence. *Phys. Rev. Lett.* **59**, 783–786.

Martin, J., Ooi, A., Chong, M. & Soria, J. 1998 Dynamics of the velocity gradient tensor invariants in isotropic turbulence. *Phys. Fluids* **10**, 2336–2346.

Orszag, S. & Patterson, G. J. 1972 Numerical simulation of three-dimensional homogeneous isotropic turbulence. *Phys. Rev. Lett.* **28**, 76–79.

Perry, A. E. & Chong, M. S. 1987 A description of eddying motions and flow patterns using critical-point concepts. *Ann. Rev. Fluid Mech.* **19**, 125–155.

Perry, A. E. & Chong, M. S. 1994 Topology of flow patterns in vortex motions and turbulence. *Appl. Sci. Res.* **53**, 357–374.

Seyed, S. & Veeravalli, S. 1994 Local isotropy in turbulent boundary layers at high Reynolds number. *J. Fluid Mech.* **268**, 333–372.

She, Z., Jackson, E. & Orszag, S. 1991 Structure and dynamics of homogeneous turbulence: models and simulations. *Proc. R. Soc. Lond.* A **434**, 101–124.

Siggia, E. & Patterson, G. 1978 Intermittency effects in a numerical simulation of stationary three-dimensional turbulence. *J. Fluid Mech.* **86**, 567–592.

Soria, J. & Cantwell, B. J. 1994 Topological visualisation of focal structures in free shear flows. *Appl. Sci. Res.* **53**, 375–386.

Soria, J., Sondergaard, R., Cantwell, B. J., Chong, M. S. & Perry, A. E. 1994 A study of the fine-scale motions of incompressible time-developing mixing layers. *Phys. Fluids* **6**, 871–884.

Sullivan, N., Mahalingam, S. & Kerr, R. 1994 Deterministic forcing of homogeneous, isotropic turbulence. *Phys. Fluids* **6**, 1612–1614.

Truesdell, C. 1954 *The Kinematics of Vorticity*. Indiana University Press.

Vieillefosse, P. 1984 Internal motion of a small element of fluid in an inviscid flow. *Physica* **125A**, 150–162.

Vincent, A. & Meneguzzi, M. 1991 The spatial structure and statistical properties of homogeneous turbulence. *J. Fluid Mech.* **225**, 1–20.

Yeung, P. 1994 Direct numerical simulation of two-particle relative diffusion in isotropic turbulence. *Phys. Fluids* **6**, 3416–3428.

YEUNG, P., GIRIMAJI, S., & POPE, S. 1988 Eulerian and Lagrangian statistics from a high-resolution direct simulation of stationary homogeneous turbulence. *Tech. Rep.* FDA-88-02. Sibley School of Mech. & Aero. Engng., Cornell University.

YEUNG, P. & POPE, S. B. 1989 Lagrangian statistics from direct numerical simulations of isotropic turbulence. *J. Fluid Mech.* **207**, 531–586.